

Optics of Solar Concentrators. Part II: Models of Light Collection of 3D-CPCs under Direct and Collimated Beams

Antonio Parretta^{1,*}, Andrea Antonini²

¹ENEA C.R. "E. Clementel", Via Martiri di Monte Sole 4, Bologna (BO), 40129, Italy

²IIT - Istituto Italiano di Tecnologia, via Morego 30, Genova (GE), 16163, Italy

Abstract The optical properties of nonimaging solar concentrators irradiated in a direct mode by collimated beams are investigated in detail adopting original simulation methods. The adopted methods were not limited to investigate useful properties for the practical application of the concentrators, but were also used to know any aspect of them regarded as generic optical elements with specific transmission, reflection and absorption characteristics. We have investigated therefore, besides the transmitted flux to the solar cell receiver, also the flux back reflected from input aperture and the flux absorbed on the wall of the concentrator. The main results of the simulations were the transmission, reflection and absorption efficiencies, the average number of reflections of the transmitted or reflected rays, their angular divergence and the distribution of flux on the receiver or on the internal wall surface. The presented methods can be fruitfully applied to any other type of solar concentrator.

Keywords Solar Concentrator, Light Collection, Optical Simulation, Optical Modeling, Nonimaging Optics

1. Introduction

A review of the theoretical models of light irradiation and collection in solar concentrators (SC) was presented in the first part of this work[1]. In this second part, we present the first optical simulations of those models, focusing our attention on the optical collection properties of nonimaging SC irradiated by direct and collimated beams. The importance of this irradiation lies in the fact that it represents the typical operating condition of a SC. We have chosen, for the optical simulations, a class of nonimaging SC of the type 3D-CPC (Three-Dimensional Compound Parabolic Concentrators) to be used mainly as primary elements of a concentrator system. The results of our work can be extended also to CPC used as secondary elements of concentration, even if subsequent parts of this work, investigating irradiation by diffuse light, could be more suitable for this application. Our interest on these SC is that they allow to reach very high concentration levels, comparable to the theoretical ones, and that their optical transmission efficiency is quite constant within a defined angle of incidence of the collimated beam. A further advantage of these SC is that they operate with reflective

surfaces, that do not induce the spectral dispersion of light.

We have simulated the optical behavior of the nonimaging SC by investigating its transmission, reflection and absorption properties. In particular, we have examined: i) the transmitted flux in terms of the optical transmission efficiency, average number of internal reflections of the transmitted rays, spatial distribution of the flux density at the exit aperture, number of reflections, angular distribution of radiance; ii) the flux reflected from the input aperture in terms of reflection efficiency, angular divergence, average number of reflections and symmetry of the radiance distribution; iii) the absorbed flux in terms of absorption efficiency and distribution of the absorbed flux on the internal wall of the CPC. In this way, all the optical features of the SC, considered as a generic optical element interacting with a direct and collimated beam, were analyzed. The methods of simulation and elaboration of the optical data presented in this work can be considered as general tools for the analysis of any other optical device.

2. The Compound Parabolic Concentrator (CPC)

The Compound Parabolic Concentrator (CPC) is a nonimaging concentrator developed by R. Winston[2] to efficiently collect Cherenkov radiation in high energy experiments. Since then, the nonimaging concentrators have been widely used to concentrate sunlight[3-16]. The CPC is

* Corresponding author:

aparretta@alice.it (Antonio Parretta)

Published online at <http://journal.sapub.org/optics>

Copyright © 2013 Scientific & Academic Publishing. All Rights Reserved

a reflective concentrator with parabolic profile and is characterized by a quasi step-like transmission efficiency (see Fig. 1) allowing the efficient collection of light from 0° to a maximum angle, called the acceptance angle θ_{acc} . A 3D-CPC is characterized by the following parameters: a = radius of entrance aperture; a' = radius of exit aperture; L = length; θ_{acc} = acceptance (or tilt) angle; f = focal length of the parabolic profile. An ideal (canonical) 3D-CPC is completely determined by two of the above five parameters, related by the following basic relationships:

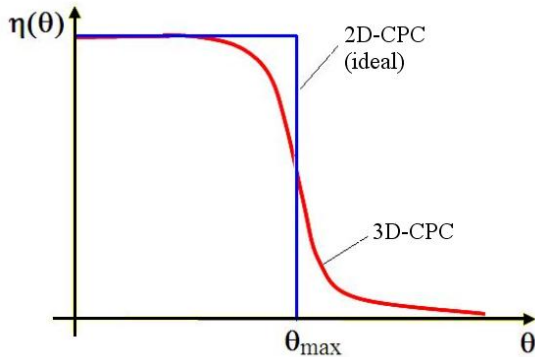


Figure 1. Example of transmission efficiency curve of the 3D-CPC, compared to the ideal (squared) curve of a 2D-CPC

$$f = a'(1 + \sin \theta_{acc}) \tag{1}$$

$$a' = a \cdot \sin \theta_{acc} \tag{2}$$

$$L = (a + a') \cdot \text{ctg} \theta_{acc} \tag{3}$$

The construction of a 3D-CPC is very simple. We can start fixing, for example, the dimension of exit aperture, with

radius a' , and the focal length, f ; the acceptance angle θ_{acc} is derived directly from Eq. (1), but can be also obtained by the following geometric construction. We start drawing the longitudinal cross section of the 3D-CPC on the x/z plane (see Fig. 2).

On a Cartesian plane x/z the projected exit aperture of the CPC, with diameter F_1 – F_2 , is aligned along the x -axis and centered on the origin O . Now we draw the parabola p_1 with upward concavity, focal length f and focus on $F_1(-a', 0)$ (see Fig. 2). The parabola p_1 is then rotated counter clockwise (CCW) around the axis perpendicular to the x/z plane and passing through F_1 , until it touches the point F_2 . The corresponding angle of rotation is the acceptance angle θ_{acc} . The positive segment of the rotated parabola p'_1 is the right profile of the CPC, intersected by the x/z plane. The left profile of the CPC is obtained starting from a second parabola with focus on F_2 and rotating it clockwise (CW), and is the specular image of p'_1 respect to the z axis.

To obtain the equation of the CPC profile, we start from the equation of parabola p_1 aligned to the z axis:

$$z(x) = \left[\frac{(x + a')^2}{4 \cdot f} - f \right] \tag{4}$$

The CCW rotation of the parabola is equivalent to the CW rotation of the x/z axes. The rotated axes, x'/z' , are related to the fixed ones by the relationships:

$$\begin{aligned} x' &= x \cdot \cos \theta_{acc} - z(x) \cdot \sin \theta_{acc} - a'(1 - \cos \theta_{acc}) \\ z' &= x \cdot \sin \theta_{acc} + z(x) \cdot \cos \theta_{acc} + a' \cdot \sin \theta_{acc} \end{aligned} \tag{5}$$

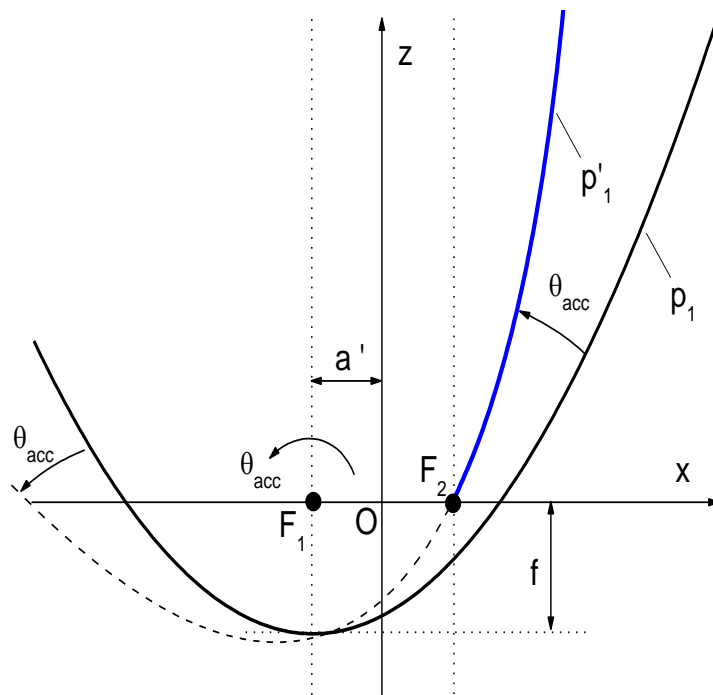


Figure 2. Basic scheme of construction of an ideal 3D-CPC

The rotated profile of the CPC can be obtained calculating the new coordinates from Eq. (5); this allows to quick draw the profile by numerical simulation. To better manipulate the CPC profile, however, it is convenient deriving an analytical expression of the new coordinates: $z' = z'(x')$. By using Eq. (4), the x and z coordinates can be eliminated from Eq. (5) and the analytical expression of the new coordinates: $z' = z'(x')$ becomes:

$$z' = d \cdot w(x') - e \cdot \sqrt{w(x')} + g \quad (6)$$

where d , e and g are constant quantities:

$$d = \frac{\cos \theta_{acc}}{16f \cdot \sin^2 \theta_{acc}} \quad (7)$$

$$e = \frac{1}{2} + \frac{2b \cdot \cos \theta_{acc}}{16f \cdot \sin^2 \theta_{acc}} + \frac{a' \cdot \cos \theta_{acc}}{4f \cdot \sin \theta_{acc}} \quad (8)$$

$$g = \frac{b}{2} + \frac{b^2 \cdot \cos \theta_{acc}}{16f \cdot \sin^2 \theta_{acc}} + \frac{a'^2 \cdot \cos \theta_{acc}}{4f} + \frac{a' \cdot b \cdot \cos \theta_{acc}}{4f \cdot \sin \theta_{acc}} + \dots \quad (9)$$

$$\dots + a' \cdot \sin \theta_{acc} - f \cdot \cos \theta_{acc}$$

where also b and c are constant quantities:

$$b = 4f \cdot \cos \theta_{acc} - 2a' \cdot \sin \theta_{acc} \quad (10)$$

$$c = (a')^2 \cdot \sin \theta_{acc} - 4f^2 \cdot \sin \theta_{acc} + 4f \cdot a' \cdot (1 - \cos \theta_{acc}) \quad (11)$$

and the function $w(x')$ is given by:

$$w(x') = b^2 - 4 \cdot (4f \cdot x' + c) \cdot \sin \theta_{acc} \quad (12)$$

Eqs. (6-12) allow to calculate the slope of the CPC curve at any point. In particular, we look for the point where the tangent is parallel to the z' axis. This point defines the upper limit of the CPC profile, that is the maximum length L of the CPC, then it also defines the maximum value of the input

opening radius, a (see Fig. 3). By deriving Eq. (6) we have:

$$\frac{dz'}{dx'} = \frac{dz'}{dw} \cdot \frac{dw}{dx'} = \dots \quad (13)$$

$$\dots = \left[\frac{e}{2\sqrt{b^2 - 4 \cdot (4f \cdot x' + c) \cdot \sin \theta_{acc}}} - d \right] \cdot (16f \cdot \sin \theta_{acc})$$

The condition for a tangent to the curve parallel to z' axis is:

$$\frac{dz'}{dx'} = \infty \Rightarrow b^2 - 4 \cdot (4f \cdot x' + c) \cdot \sin \theta_{acc} = 0 \quad (14)$$

$$\Rightarrow x' = x'(L) = \frac{f - a' \sin \theta_{acc}}{\sin \theta_{acc}} = \frac{a'}{\sin \theta_{acc}} = a$$

The profile of the CPC ends at the $z' = L$, corresponding to the point A of Fig. 3, where the tangent to the profile is parallel to the z' axis. The surface of the 3D-CPC is finally constructed by turning the left and right profiles of the angle π around the z' axis.

As a consequence of this construction, two extreme rays (1 and 2 in Fig. 3) incident at θ_{acc} and crossing the z' axis (meridian rays), will be both collected at F_1 . It can be demonstrated that all the meridian rays incident at $\theta \leq \theta_{acc}$ will be collected, whereas some of the non meridian rays incident at $\theta \leq \theta_{acc}$ will not be collected, and some of the non meridian rays incident at $\theta \geq \theta_{acc}$ angle will be collected. The result is the transmission efficiency curve for the 3D-CPC as reported in Fig. 1 (red curve). In a 2D-CPC all the rays are meridian[2], then they will be all collected at $\theta \leq \theta_{acc}$ (see the blue curve of Fig. 1).

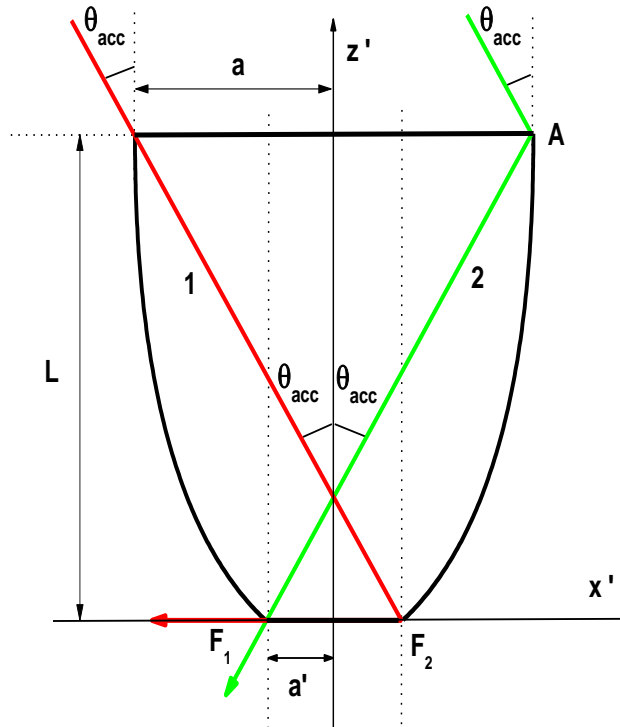


Figure 3. Longitudinal cross section profile of the 3D-CPC

For the optical simulations, we have used an ideal (not truncated) 3D-CPC for which we have chosen the following two independent parameters: $\theta_{acc} = 5^\circ$, $L = 150$ mm. From Eqs. (2) and (3) we derive: $a = 12.035$ mm, $a' = 1.052$ mm and from Eq. (1) we derive: $f = 1.14$ mm. The only change made to the concentrator during the optical simulations was that of reflectance of the internal wall; all the other added devices (absorbers, screens, etc.) were external to the concentrator and were used as tools to improve the knowledge of its optical properties. All the optical simulations were carried out by using the TracePro ray-tracing software of Lambda Research[17].

3. Analysis of the Transmitted Flux

3.1. Optical Transmission Efficiency

To simulate the optical transmission curve $\eta_\tau(\theta_{in})$ under direct irradiation of the 3D-CPC defined in the previous section, we irradiate it by a parallel and uniform beam investing the entire surface of input aperture. To illustrate how the TracePro software is operating, Fig. 4 shows two examples of the 3D-CPC with ideal internal walls (unitary reflectivity) irradiated by a parallel beam incident at $\theta_{in} = 0^\circ$ (a) and $\theta_{in} = \theta_{acc} = 5^\circ$ (b). An ideal absorber is placed as receiver at the output. For $\theta_{in} = 0^\circ$ all the incident rays are collected by the receiver ($\eta_\tau(0) = 1$). For $\theta_{in} = \theta_{acc}$, instead, we see that a portion of rays, exactly half of them, are back reflected by the CPC, as required by definition of θ_{acc} .

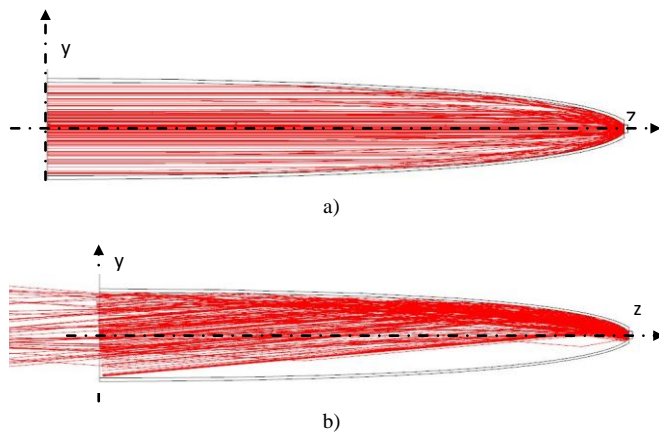


Figure 4. Irradiation of an ideal 3D-CPC, with $\theta_{acc} = 5^\circ$, by a parallel beam inclined at $\theta_{in} = 0^\circ$ (a) and at $\theta_{in} = 5^\circ$ (b)

The TracePro software allows to select a source of light (in this case a parallel beam), and to put it in the chosen place (in this case at the input aperture of the CPC) and directed towards the chosen direction (in this case towards the CPC). To draw the transmission efficiency curve of the CPC at various operating conditions, we need to irradiate it at different angles of incidence, θ_{in} , assigning different values

to the wall reflectivity, R_w . The transmission efficiency is then defined as the ratio between the output and input flux:

$$\eta_\tau(\theta_{in}, R_w) = \frac{\Phi_{out}(\theta_{in}, R_w)}{\Phi_{in}} \quad (15)$$

The input flux is assigned by the number of input rays and by the flux of the single ray (generally 1 W); the output flux is obtained by measuring the total flux incident on the ideal absorber placed at the output, and the software gives also the number of rays associated to the output flux. Three transmission efficiency curves were obtained at three different values of R_w : 1.0, 0.9, 0.8. The three curves are shown in Fig. 5.

Fig. 5 shows that the $\eta_\tau(R_w, \theta_{in})$ curves maintain the step-like shape with the same $\theta_{acc} = 5^\circ$ value at decreasing R_w , but the efficiency values are lowered. The lowering is about 20% when R_w is lowered of about the 10%, and is about 40% when R_w is lowered of about the 20%. This means that the rays inside the CPC make, on average, two reflections. From Fig. 5 we note also that the $\eta_\tau(R_w, \theta_{in})$ curves have a hump for $R_w < 1$, then we expect that the number of reflections has a depression for the central values of the incidence angle. The details of the behavior of number of reflections inside the CPC can be obtained by comparing at least two of the $\eta_\tau(R_w, \theta_{in})$ curves of Fig. 5. This will be done in section 3.3. In the following section we will have a look at the flux distribution on the exit aperture.

3.2. Distribution of the Flux at the Exit Aperture

The flux distribution, or irradiance, at the output of the CPC is obtained analyzing the flux on the absorber closing the exit aperture. Here we make only a qualitative investigation of the output flux limiting our attention to the CPC with ideal internal walls (no optical loss by absorptance). Fig. 6 shows a series of maps of the output flux taken at eight values of the incidence angle of the collimated beam: $\theta_{in} = 0.0^\circ$; 1.0° ; 2.0° ; 3.0° ; 4.0° ; 4.75° ; 5.0° ; 5.50° . The output flux shows a rotational symmetry, the same of the CPC, at $\theta_{in} = 0^\circ$, with a strong peak at the center.

Increasing θ_{in} , the flux moves to one side of the output, the upper one in Fig. 6, and at 3° it takes the form of a "crab". For $\theta_{in} > 3^\circ$ the flux moves to the other side of the output, the lower one in Fig. 6, and at $\theta_{in} \approx \theta_{acc} = 5^\circ$ it is fully distributed on one half of the exit opening. For $\theta_{in} > \theta_{acc}$ the flux decreases significantly, tending to be distributed on the output opening edge. This behavior will be revised when, in a forthcoming part of this work, we will talk about the "local" optical efficiency of the concentrator. We have verified that, reducing R_w from 1.0 to 0.8, does not change appreciably the flux distribution at the output.

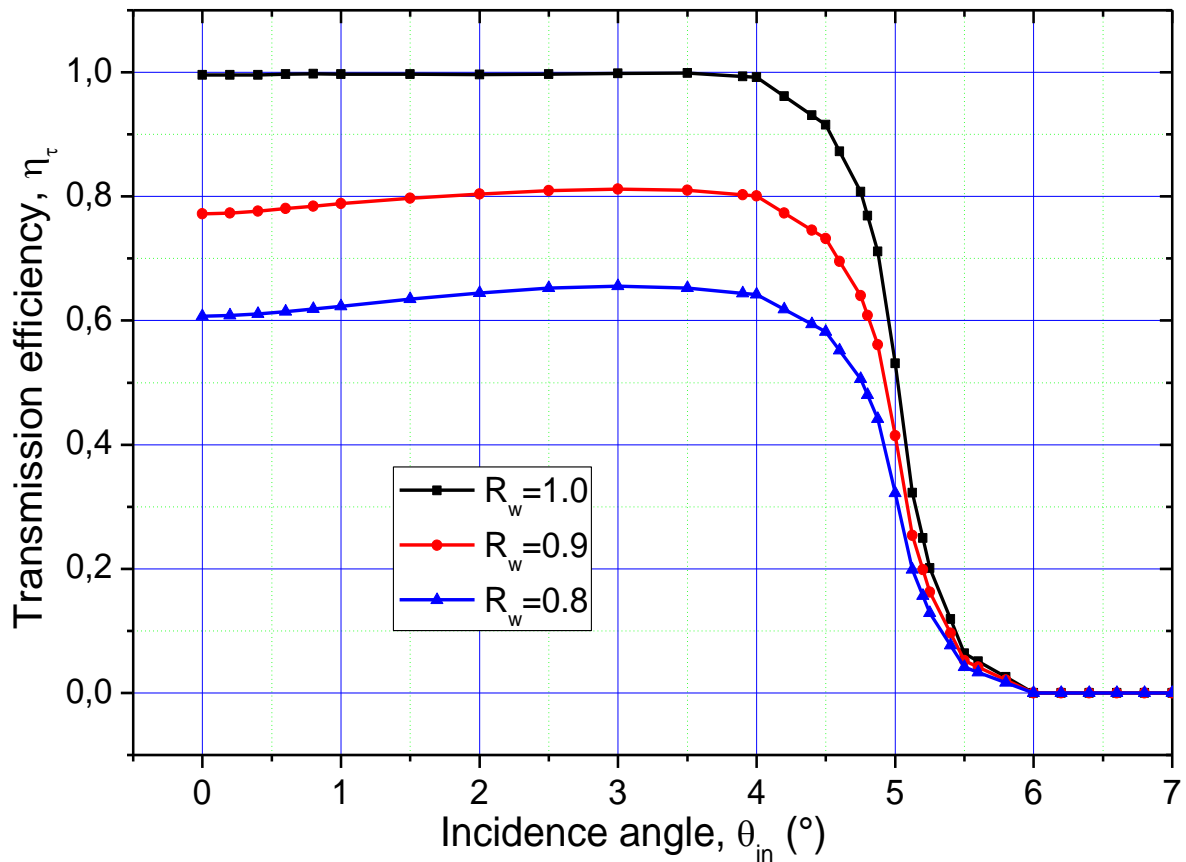
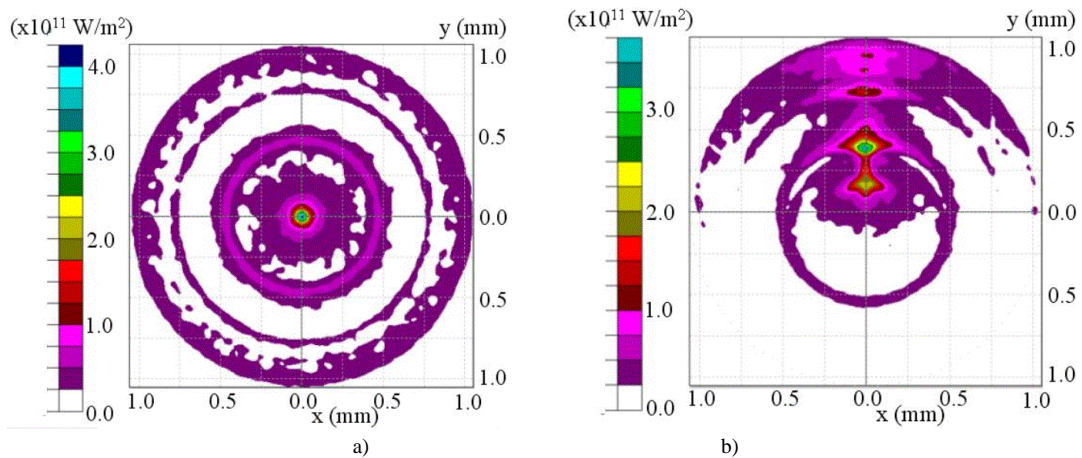


Figure 5. Optical transmission efficiency $\eta_{\tau}(\theta_{in}, R_w)$ of the 3D-CPC calculated for three wall reflectivities: $R_w = 1.0, 0.9$ and 0.8

The map of irradiance at $\theta_{in} = 0^\circ$ shows that a high concentration of flux is present at the center of the output aperture. This is direct consequence of the 3D-CPC symmetry. This condition of operation is not tolerable if the CPC is used as primary concentrating unit in a PV system. The receiver of a PV system, a solar cell or a solar module, in fact, cannot operate with strong inhomogeneous fluxes[18-21]. The maximum tolerated deviation from the average flux density is about 100%, very far lower than what measured at $\theta_{in} = 0^\circ$ (see Fig. 9). The way to overcome this problem is to break the symmetry of the CPC. This can be done by using a secondary optical element (a prism) coupled to the CPC output[15, 16, 22-27], or deforming the CPC wall surface maintaining almost unchanged its transmission efficiency and concentration properties[9].



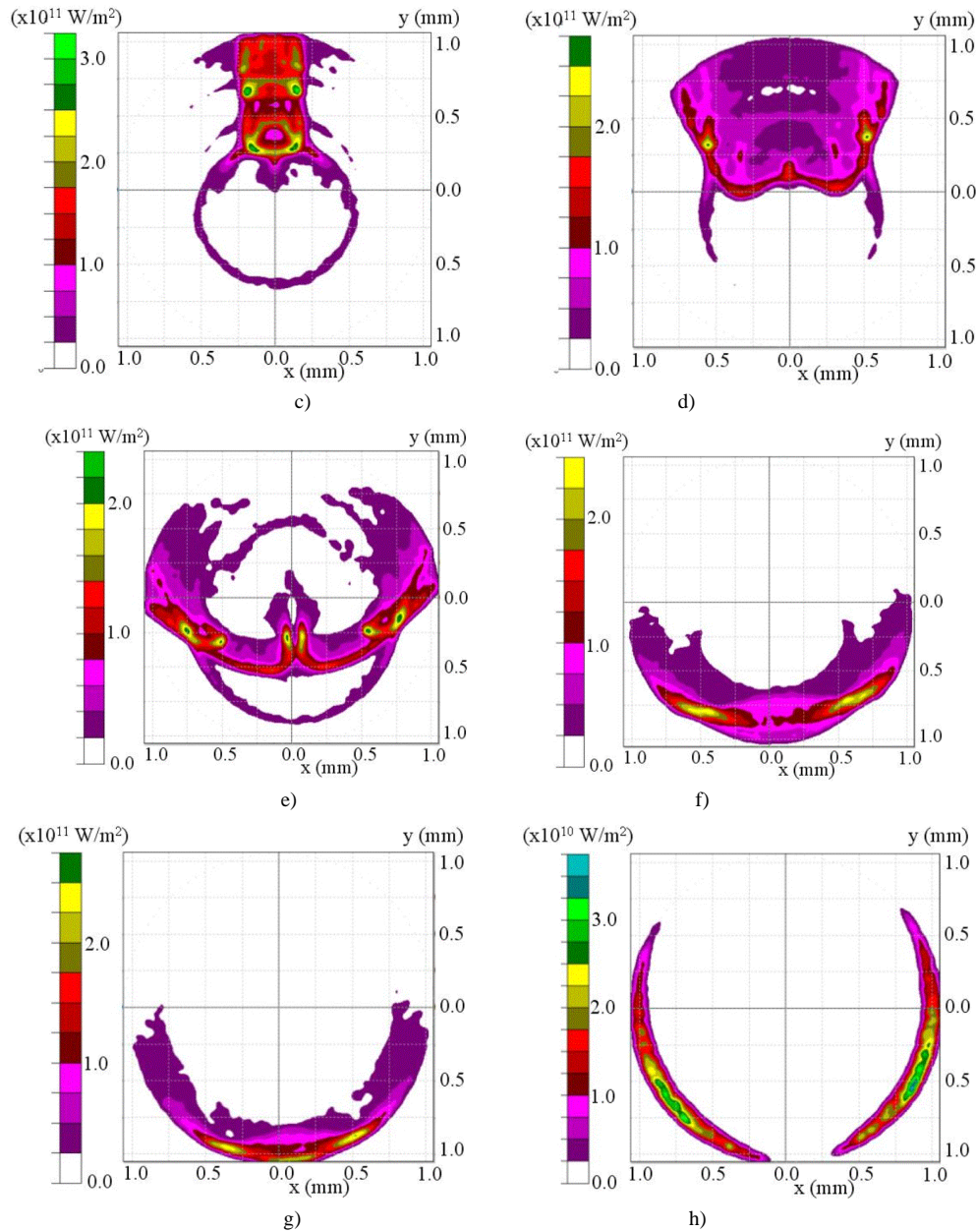


Figure 6. Maps of output flux on the absorber for nine values of incidence angle of the collimated beam at input: $\theta_{in} = 0.0^\circ$ (a); 1.0° (b); 2.0° (c); 3.0° (d); 4.0° (e); 4.75° (f); 5.0° (g); 5.50° (h). Number of input rays: 100k

3.3. Number of Internal Reflections of the Transmitted Rays

When a bundle of rays is involved in a single process, like only transmission or only reflection, and undergoes an optical attenuation on the wall of the concentrator, with known reflectivity R_w , the average number of reflections \bar{N} of the rays can be easily calculated by comparing the input flux Φ_{in} with the output flux Φ_{out} :

$$\Phi_{out} = \Phi_{in} \cdot (R_w)^{\bar{N}} \quad (16)$$

From Eq. (16) the quantity \bar{N} can be immediately calculated. Eq. (16), however, cannot be applied alone when both transmitted and reflected rays are present, because the

portion of input flux associated to the transmission or to the reflection processes it is not known “a priori”. In the actual case, where we have both transmitted and reflected rays (the CPC is made of two exit apertures), to know the average number of reflections the rays make on the internal wall before being collected, it is required the knowledge of the output flux or efficiency of the considered process to at least two wall reflectivities. We have therefore to apply two equations, that, in the case of reflected rays, become:

$$\Phi'_{out} = \Phi_{in}^{\rho} \cdot (R'_w)^{\bar{N}_{\rho}} \quad (17a)$$

$$\Phi''_{out} = \Phi_{in}^{\rho} \cdot (R''_w)^{\bar{N}_{\rho}} \quad (17b)$$

The input flux Φ_{in}^{ρ} is not known, but the measure of the

output flux Φ_{out} at two values of the wall reflectivity, R'_w and R''_w , is sufficient to know the correct value of \bar{N}_ρ .

Fig. 7 shows the scheme of the CPC irradiated by a collimated beam, with E_{dir} perpendicular irradiance, inclined at θ_{in} angle respect to the optical axis z . We define the following quantities:

- θ_{in} : polar incidence angle of the input ray or beam;
- ϕ_{in} : azimuthal incidence angle of the input ray;
- P : point of the input aperture;
- Φ_{in} : flux of the input beam;
- N_{in} : number of rays at input;
- ϕ_{in} : flux of the single ray at input;
- Φ_τ : output or “transmitted” flux;
- N_τ : output or “transmitted” number of rays;
- Φ_ρ : flux reflected at input;
- N_ρ : number of reflected rays;

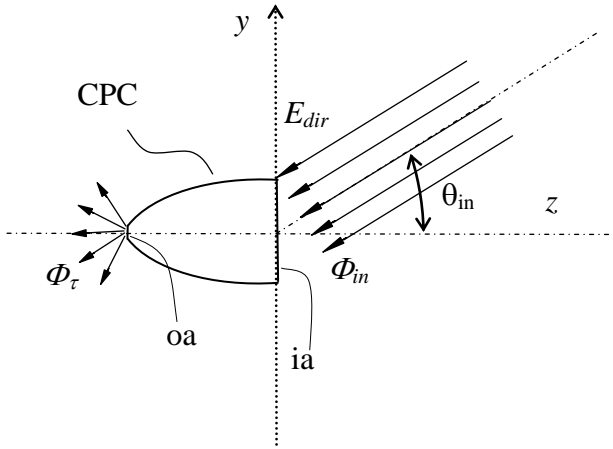


Figure 7. Basic scheme of the 3D-CPC irradiated by a collimated beam

- $\bar{\phi}_\tau$: average flux of the transmitted ray;
 - $\bar{\phi}_\rho$: average flux of the reflected ray;
 - \mathcal{N}_i : number of reflections of the i^{th} transmitted ray;
 - \bar{N}_τ : average number of reflections of the transmitted rays;
 - \mathcal{N}_j : number of reflections of the j^{th} reflected ray;
 - \bar{N}_ρ : average number of reflections of the reflected rays;
 - η_τ : transmission efficiency;
 - R_w : wall reflectivity.
- The variable quantities are those dependent on R_w and θ_{in} : $\Phi_\tau = \Phi_\tau(R_w, \theta_{in})$; $N_\tau = N_\tau(R_w, \theta_{in})$; $\Phi_\rho = \Phi_\rho(R_w, \theta_{in})$; $N_\rho = N_\rho(R_w, \theta_{in})$; $\mathcal{N}_i = \mathcal{N}_i(\theta_{in}, \phi_{in}, P)$; $\bar{N}_\tau = \bar{N}_\tau(R_w, \theta_{in})$; $\mathcal{N}_j = \mathcal{N}_j(\theta_{in}, \phi_{in}, P)$; $\bar{N}_\rho = \bar{N}_\rho(R_w, \theta_{in})$; $\eta_\tau = \eta_\tau(R_w, \theta_{in})$.

We have for the input flux:

$$\Phi_{in} = N_{in} \cdot \phi_{in} \quad (18)$$

The transmitted flux can be expressed as follows:

$$\Phi_\tau(R_w, \theta_{in}) = \sum_{i=1}^{N_{in}} \phi_{in} \cdot (R_w)^{\mathcal{N}_i(\theta_{in}, \phi_{in}, P)} = \dots \quad (19)$$

$$\dots = N_\tau(R_w, \theta_{in}) \cdot \phi_{in} \cdot (R_w)^{\bar{N}_\tau(R_w, \theta_{in})}$$

In Eq. (19) the number of reflections of the i -th ray, \mathcal{N}_i , requires the information about the direction (polar θ_{in} and azimuthal ϕ_{in}) and the point P of impact on the input aperture. The average number of reflections \bar{N} , instead, requires only the information about the polar angle θ_{in} , having the CPC a cylindrical symmetry. In Eq. (19), however, \bar{N} has been expressed also as function of the wall reflectivity. This, in principle, should not be so. The fact is that the software operates by introducing a threshold on the output flux of the single ray, below which the ray is removed from the count of the output rays (transmitted or reflected). The threshold applied by the software in the actual case is 5% of the starting flux, and could not be reduced[17]. The effect of the threshold on \bar{N} is to lower it at lowering R_w , because for lower R_w values more rays are removed, those bringing the information of high reflections, then the average of \bar{N} lowers.

Substituting the transmitted flux $\Phi_\tau(R_w, \theta_{in})$ of Eq. (19) in the expression of the transmission efficiency of Eq. (15) we obtain:

$$\begin{aligned} \eta_\tau(R_w, \theta_{in}) &= \frac{\Phi_\tau(R_w, \theta_{in})}{\Phi_{in}} = \dots \\ &= \frac{N_\tau(R_w, \theta_{in}) \cdot (R_w)^{\bar{N}_\tau(R_w, \theta_{in})}}{N_{in}} \end{aligned} \quad (20)$$

If the transmission efficiency of Eq. (20) is measured for two different wall reflectivities, R'_w and R''_w , we obtain for their ratio:

$$\begin{aligned} \frac{\eta_\tau(R'_w, \theta_{in})}{\eta_\tau(R''_w, \theta_{in})} &= \frac{\Phi_\tau(R'_w, \theta_{in})}{\Phi_\tau(R''_w, \theta_{in})} = \dots \\ &= \frac{N_\tau(R'_w, \theta_{in}) \cdot (R'_w)^{\bar{N}_\tau(R'_w, \theta_{in})}}{N_\tau(R''_w, \theta_{in}) \cdot (R''_w)^{\bar{N}_\tau(R''_w, \theta_{in})}} \end{aligned} \quad (21)$$

When two closed values are chosen for the wall reflectivities, we can assume that the average number of reflections remains almost constant, then we can introduce the average quantity:

$$\bar{N}_\tau(R'_w, R''_w, \theta_{in}) \approx \frac{\bar{N}_\tau(R'_w, \theta_{in}) + \bar{N}_\tau(R''_w, \theta_{in})}{2} \quad (22)$$

Eq. (21) can be written as:

$$\frac{\eta_\tau(R'_w, \theta_{in})}{\eta_\tau(R''_w, \theta_{in})} \approx \frac{N_\tau(R'_w, \theta_{in})}{N_\tau(R''_w, \theta_{in})} \cdot \left[\frac{R'_w}{R''_w} \right]^{\bar{N}_\tau(R'_w, R''_w, \theta_{in})} \quad (23)$$

From Eq. (23) we finally obtain the expression for the average number of reflections of the transmitted rays:

$$\bar{N}_\tau(R'_w, R''_w, \theta_{in}) \approx \frac{\log \left[\frac{\eta_\tau(R'_w, \theta_{in}) \cdot N_\tau(R''_w, \theta_{in})}{\eta_\tau(R''_w, \theta_{in}) \cdot N_\tau(R'_w, \theta_{in})} \right]}{\log \left[\frac{R'_w}{R''_w} \right]} \quad (24)$$

Eq. (24) gives the average number of reflections for two neighboring values R'_w and R''_w of wall reflectivity. The quantity $\bar{N}_\tau(R'_w, R''_w, \theta_{in})$ reduces when the wall reflectivities reduce, because the more attenuated rays, those undergoing more reflections, can be attenuated so much to be unable to reach the output aperture, so they are not counted in the number of transmitted rays. Eq. (24) can be applied only when the output number of rays is known. As we will see later, not all the simulations aimed to obtain $\bar{N}_\tau(R'_w, R''_w, \theta_{in})$ allow to obtain also the number of rays at output, so we must introduce a further approximation in Eq. (24) by assuming that the number of rays at output is almost constant. Then Eq. (24) becomes:

$$\bar{N}_\tau(R'_w, R''_w, \theta_{in}) \approx \frac{\log \left[\frac{\eta_\tau(R'_w, \theta_{in})}{\eta_\tau(R''_w, \theta_{in})} \right]}{\log \left[\frac{R'_w}{R''_w} \right]} \quad (25)$$

Eq. (24) can be applied only by using “direct methods” of irradiation of the concentrator, that is irradiation of the input

aperture. Further investigations will be used by applying “inverse methods” of irradiation, that is irradiation of the output aperture; for these methods we will use Eq. (25) to estimate $\bar{N}_\tau(R'_w, R''_w, \theta_{in})$, as the number of output rays is unknown in this last case.

We use now the three curves of transmission efficiency of Fig. 5, obtained at $R_w = 1.0, 0.9$ and 0.8 , to simulate the number of reflections of rays inside the 3D-CPC. We have calculated $\bar{N}_\tau(R'_w, R''_w, \theta_{in})$ for the following three pairs of reflectivities: $(1.0; 0.9)$, $(1.0; 0.8)$, $(0.9; 0.8)$, which cover the range of realistic values obtained in practice. Fig. 8 shows the curves of $\bar{N}_\tau(R'_w, R''_w, \theta_{in})$ obtained applying Eq. (24).

First of all, we find that the rays inside the CPC make about two reflections, on average, as inferred commenting on the curves of transmission efficiency of Fig. 5; also the depression of \bar{N}_τ observed at the center of the angular interval has been inferred by looking at the same curves. We note from Fig. 8 that, as expected, the number of reflections slightly reduces when the values of reflectivity are reduced, because only the rays undergoing less reflections are collected at the output if the walls become more absorbing, as already discussed.

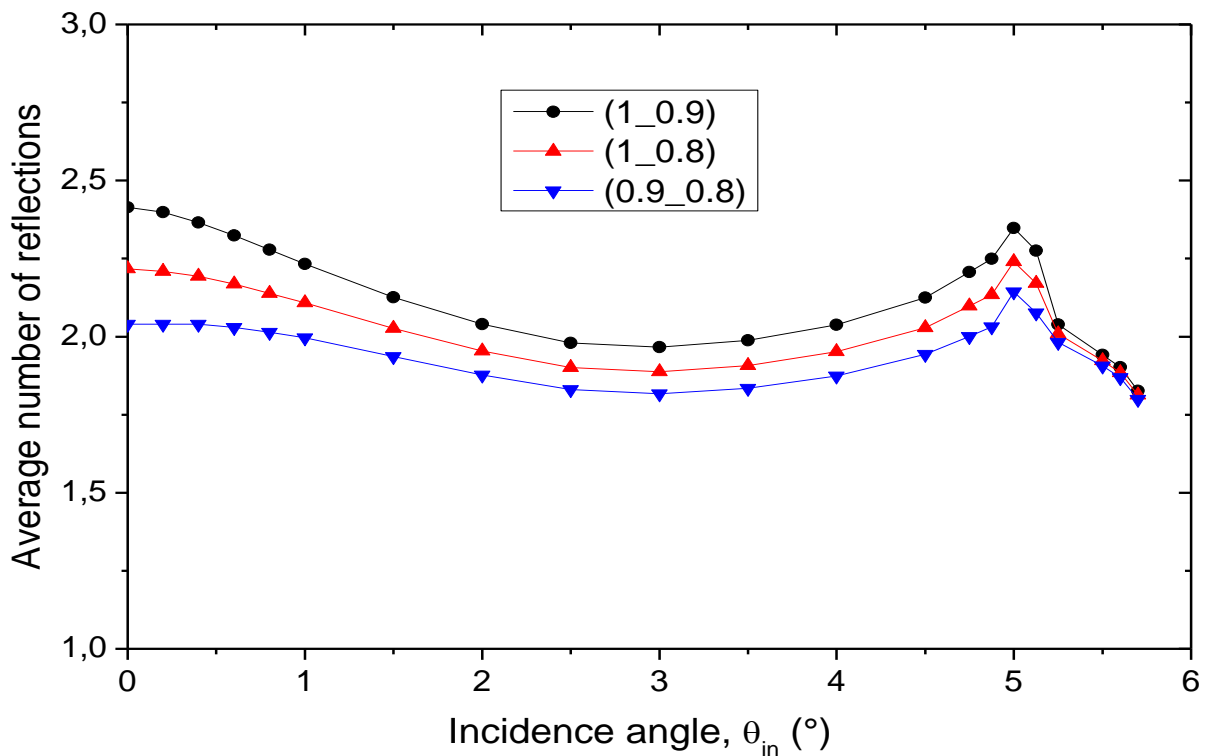


Figure 8. Curves of the average number of reflections of rays inside the CPC, simulated by applying Eq. (24) for three different pairs of values of internal wall reflectivity: $(R'_w, R''_w) = (1.0; 0.9)$, $(1.0; 0.8)$, $(0.9; 0.8)$

3.4. Analysis of the Output Flux

We have seen from Fig. 6a that, at 0° incidence of the parallel beam, the output flux is mainly focused on the center of the receiver. We analyze in detail the output flux distribution at this condition. The profile of the light intensity (irradiance) at the output on a meridian section of the CPC (the longitudinal section containing the optical axis) is shown in Fig. 9.

The x coordinate represents the relative distance of the point from the center of the circular receiver. Fig. 9 shows the curves of intensity for three different wall reflectivities: $R_w = 1.0, 0.9$ and 0.8 . The intensity profiles were obtained by applying the rotational symmetry to the map of the output flux. This operation allows, in fact, to recover the information at all azimuthal angles, then to have the average flux density profile. The effect of symmetrization is shown in Fig. 10.

The symmetrization clearly improves the flux density map (see Fig. 10 a, b) and the signal-to-noise ratio is clearly enhanced (see Fig. 10 c, d), and this allows to operate with a reduced number of rays.

Reducing R_w also the intensity of light on the receiver reduces due to the partial absorption of light on the wall. Fig. 10 shows that the profile is characterized, besides the high central peak, by other satellite peaks distributed on the radius of the receiver.

We aim to analyze the average number of reflections made by the rays which contribute to the formation of these peaks. To do this, we need to analyze the flux at different values of R_w , by the same procedure followed to get the average

number of reflections of rays of the parallel beam at changing the incidence angle (Fig. 8). This indeed is the general method adopted for calculating the average number of reflections. To this purpose, we use Eq. (24), after replacing the optical efficiency $\eta_\tau = \eta_\tau(R_w, \theta_{in})$ with the light intensity $I = I(x, R_w, \theta_{in})$ measured on the output at the point distant x from the center.

For a generic collimated beam incident at θ_{in} angle we have therefore:

$$\bar{N}_\tau(x, R'_w, R''_w, \theta_{in}) \approx \frac{\log \left[\frac{I(x, R'_w, \theta_{in}) \cdot N_\tau(R''_w, \theta_{in})}{I(x, R''_w, \theta_{in}) \cdot N_\tau(R'_w, \theta_{in})} \right]}{\log \left[\frac{R'_w}{R''_w} \right]} \quad (26)$$

For a parallel beam incident at 0° , as in the actual case, Eq. (26) becomes:

$$\bar{N}_\tau(x, R'_w, R''_w, 0) \approx \frac{\log \left[\frac{I(x, R'_w, 0) \cdot N_\tau(R''_w, 0)}{I(x, R''_w, 0) \cdot N_\tau(R'_w, 0)} \right]}{\log \left[\frac{R'_w}{R''_w} \right]} \quad (27)$$

When $N_{in} = 50k$, the number of rays at output for $\theta_{in} = 0^\circ$ at the different R_w values are: $N_\tau(R_w=1.0) = 49995$; $N_\tau(R_w=0.9) = 49813$; $N_\tau(R_w=0.8) = 49211$. By applying Eq. (27) to the intensity profiles of Fig. 9, we obtain $\bar{N}_\tau(x, R'_w, R''_w, 0)$ for the three pairs of wall reflectivity: $(R'_w, R''_w) = (1.0; 0.9), (1.0; 0.8), (0.9; 0.8)$, as shown in Fig. 11. The profile of $\bar{N}_\tau(x, R'_w, R''_w, 0)$ at the center of receiver ($x = 0$) is extremely flat and almost equal to 1 (precisely: 0.95, 0.92 and 0.89 for the three different pairs).

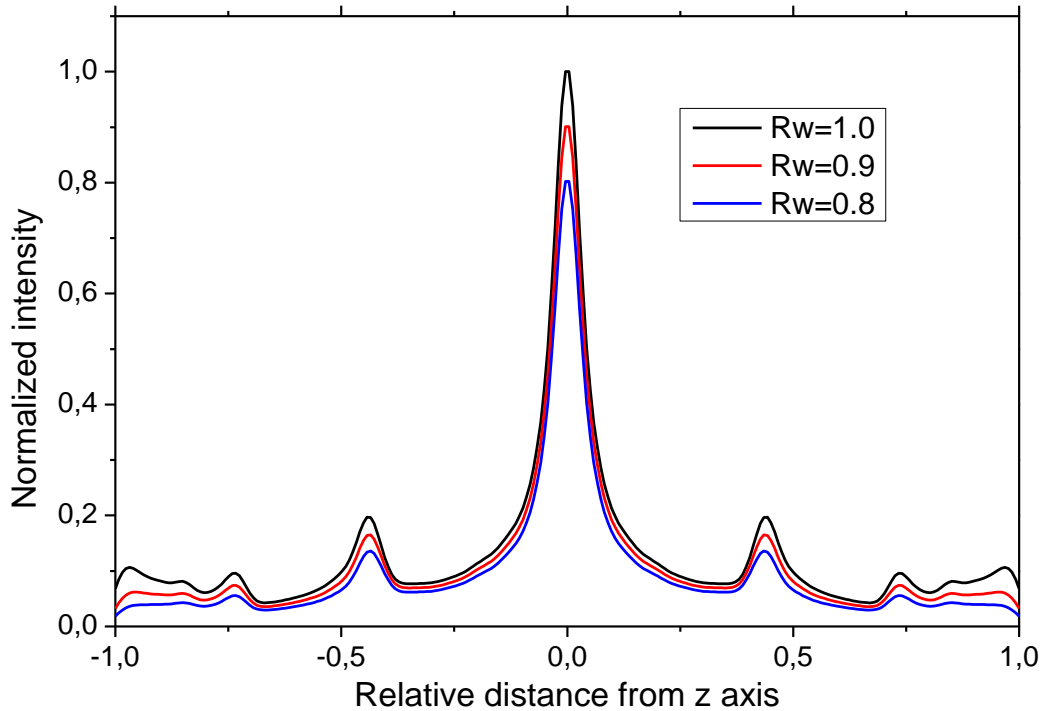
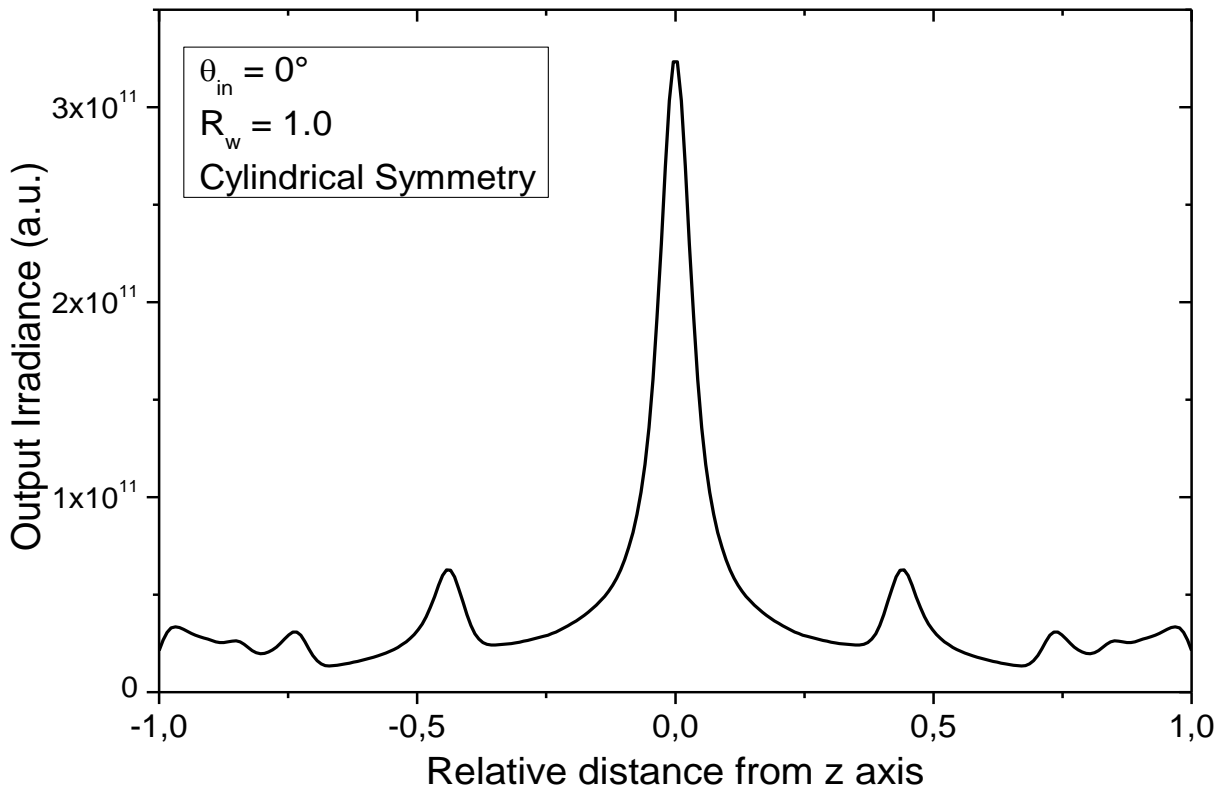


Figure 9. Intensity profiles of the flux at output of the 3D-CPC, irradiated by a collimated beam parallel to the optical axis, calculated for three different values of the internal wall reflectivity: $R_w = 1.0; 0.9$ and 0.8 . The curves have been normalized to the peak of the curve drawn at $R_w = 1.0$



d)

Figure 10. Flux density map not symmetrized (a); flux density map symmetrized (b); flux density profile of the not symmetrized map (c); flux density profile of the symmetrized map (d). Number of input rays: 100k

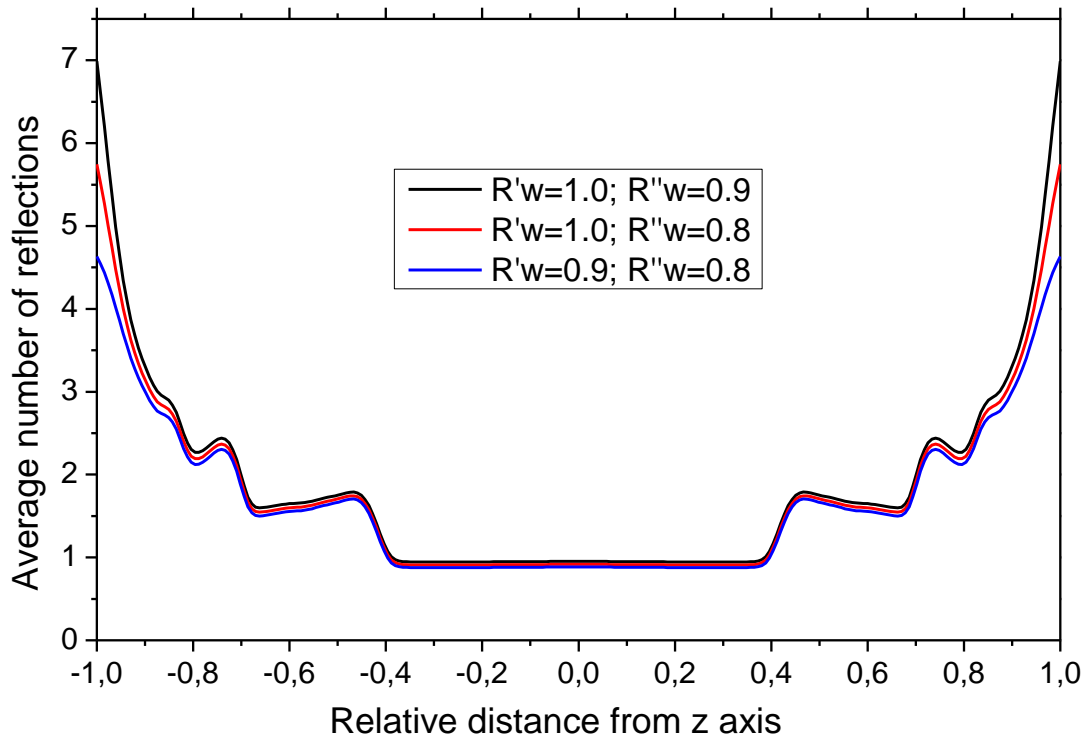


Figure 11. Average number of reflections of the rays incident on the x point of the output of the 3D-CPC, irradiated by a collimated beam parallel to the optical axis, calculated for three different pairs of wall reflectivity: $(R'_w, R''_w) = (1.0, 0.9), (1.0, 0.8), (0.9, 0.8)$

Moreover, one would expect that at the center of the receiver the average number of reflections be less than one, as the parallel rays which lie very close to the optical axis there arrive and do not undergo reflections (these are confined to $|x| \leq a'/a = 1.052/12.035 = 0.087$). Evidently, the rays arriving in the central area of the receiver are mixed so well to completely hide the contribution of those rays, for which $\mathcal{N}_\tau = 0$. We note a good matching of the three curves for $|x| \leq 0.9$, whereas, for $|x| > 0.9$ they tend to the values: ≈ 7 , ≈ 6 and ≈ 5 , respectively. The profile of $\bar{\mathcal{N}}_\tau(x, R'_w, R''_w, 0)$ is very interesting; it resembles a step-like path, with each step corresponding to one satellite peak. This is highlighted in Fig. 12 where the curve of normalized intensity for $R_w=1.0$ and of average number of reflections for $(R'_w, R''_w) = (1.0, 0.9)$ are compared.

Table 1. Peaks that appear on the profile of the flux density on the receiver of the CPC (these are just the peaks apparent, but there may be other), corresponding segment of r along the radius of the output aperture where they appear and (apparent) average number of reflections calculated for wall reflectivities $(R'_w, R''_w) = (1.0; 0.9)$. The CPC is irradiated by a parallel beam incident at 0° . The radius of the receiver is normalized to 1

Peak	r interval	$\bar{\mathcal{N}}$ reflections
I	0.0÷0.35	≈ 1
II	0.35÷0.65	≈ 1.7
III	0.65÷0.80	≈ 2.5
IV	0.80÷0.90	≈ 3
V	0.90÷1.0	≈ 5.5

From Fig. 12 we note a central peak, P_I , at $|x|=0\div 0.35$; a second peak (or first satellite), P_{II} , at $|x|=0.35\div 0.65$; a third peak (or second satellite), P_{III} , at $|x|=0.65\div 0.80$; a barely visible fourth peak (or third satellite), P_{IV} , at $|x|=0.80\div 0.90$;

and finally a fifth peak (or fourth satellite), P_V , at $|x|=0.90\div 1.0$. From Fig. 12 we see also that P_I is made of rays reflected about once, P_{II} is made of rays reflected about 1.7 times, P_{III} is made of rays reflected about 2.5 times, P_{IV} is made of rays reflected about 3 times, and P_V is made of rays reflected about 5.5 times (see Table 1, where we have used $r = |x|$).

If we calculate the average number of reflections made by all the rays reaching the receiver by integration on $|x|$ from 0 to 1:

$$\bar{\mathcal{N}}_\tau(R'_w, R''_w, 0) \approx \frac{\int_{r=0}^1 dr \cdot 2\pi r I(r, R'_w, 0) \cdot \bar{\mathcal{N}}(r, R'_w, R''_w, 0)}{\int_{r=0}^1 dr \cdot 2\pi r I(r, R'_w, 0)} = \frac{\int_{r=0}^1 dr \cdot r I(r, 0, R'_w) \cdot \bar{\mathcal{N}}(r, 0, R'_w, R''_w)}{\int_{r=0}^1 dr \cdot r I(r, 0, R'_w)} \quad (28)$$

where $r = |x|$, we find $\bar{\mathcal{N}}_\tau(0, R'_w, R''_w) = 2.41$ when $(R'_w, R''_w) = (1.0, 0.9)$, exactly the same value we have obtained by applying Eq. (24) with $\theta_{in} = 0^\circ$ (see black curve of Fig. 8 at $\theta_{in} = 0^\circ$). This result demonstrates the validity of the analytical method used by us to evaluate the number of reflections of the rays.

It is useful to evaluate the relative weight, in terms of flux, of the different peaks of the intensity profiles of Fig. 9. The relative weight of the five peaks, as function of R_w , is obtained by applying the following expressions:

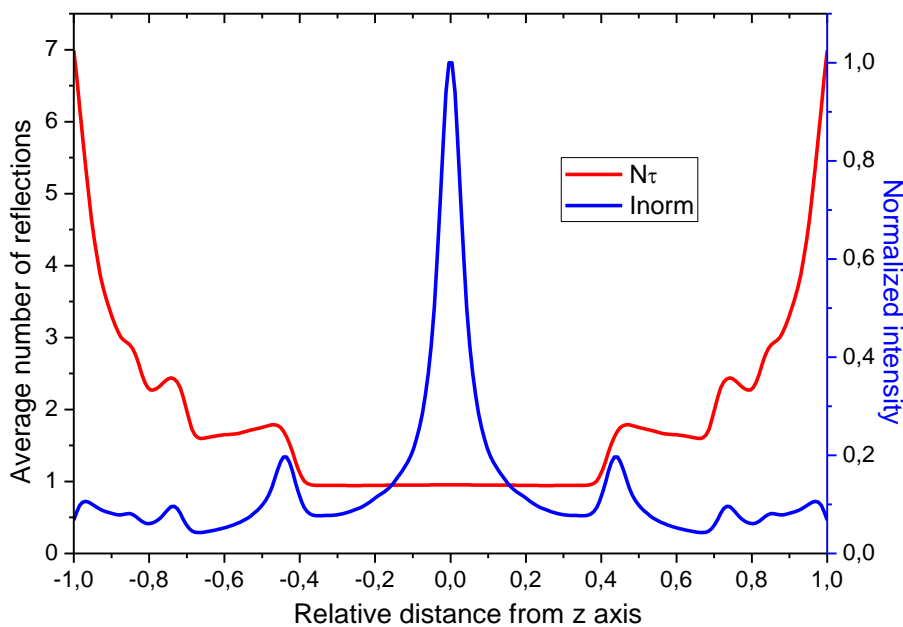


Figure 12. Comparison between the curve of normalized intensity for $R_w=1.0$ and the curve of average number of reflections for $(R'_w, R''_w) = (1.0; 0.9)$ of the rays incident on the output of the 3D-CPC, irradiated by a collimated beam parallel to the optical axis

$$P_I(R_w) = \frac{\int_{r=0}^{0.35} dr \cdot 2\pi r \cdot I(r, R_w, 0)}{1.0} \quad (29a)$$

$$P_{II}(R_w) = \frac{\int_{r=0}^{0.65} dr \cdot 2\pi r \cdot I(r, R_w, 0)}{1.0} \quad (29b)$$

$$P_{III}(R_w) = \frac{\int_{r=0}^{0.8} dr \cdot 2\pi r \cdot I(r, R_w, 0)}{1.0} \quad (29c)$$

$$P_{IV}(R_w) = \frac{\int_{r=0}^{0.9} dr \cdot 2\pi r \cdot I(r, R_w, 0)}{1.0} \quad (29d)$$

$$P_V(R_w) = \frac{\int_{r=0}^{1.0} dr \cdot 2\pi r \cdot I(r, R_w, 0)}{1.0} \quad (29e)$$

The results are summarized in Table 2.

Table 2. Relative weight in terms of flux, as function of the wall reflectivity R_w , absolute and relative area, of the three main peaks of the intensity profile at output of the CPC, when irradiated by a parallel beam incident at 0° . The radius of the receiver is normalized to 1.

Peak	Weight (%)	R_w			Area	Area rel. (%)
		1.0	0.9	0.8		
I	P_I	17.1	19.8	22.4	0.385	12.2
II	P_{II}	31.3	33.8	35.6	0.942	30.0
III	P_{III}	17.4	17.6	17.3	0.683	21.7
IV	P_{IV}	13.7	13.0	11.9	0.534	17.0
V	P_V	20.5	15.8	12.8	0.597	19.0
	Total	100.0	100.0	100.0	π	100.0

From Table 2 we see first of all that the central peak, even far higher than the others, has a minor effect in terms of flux at the receiver, only about 20%. The second peak is that one with the maximum weight, around 30%. The reason for this behavior can be found by looking at the area of the peaks. Peak P_{II} , with the maximum weight, is also that one with the maximum relative area. We note also that the weight of P_I and P_{II} increases at decreasing R_w , whereas the opposite happens for the others, in particular for P_{IV} and P_V . The reason is that P_{IV} and P_V are built with peripheral rays which are reflected, on average, more times (from ≈ 3 to ≈ 7), then

they are more attenuated respect to the other peaks at decreasing R_w . The weight of P_{IV} and P_V , therefore, decreases in favor of P_I and P_{II} .

3.5. Evolution of the Output Flux

We now study how the output flux profile evolves when the input collimated beam is parallel to the optical axis of the CPC and its cross section diameter is increased from a minimum value to the maximum value, 24 mm. In this way we will be able to know which region, with annular shape, of the input aperture, crossed by the collimated beam, is the origin of a particular intensity peak appearing on the flux profile measured at the output aperture. In this way we will see the output intensity profile growing as we are going to add more rays on the outer annulus of input beam. The cross section radius of the input beam has been varied from $R = 2$ mm to $R = 12$ mm with 1 mm steps (the radius of the input aperture is $a = 12.035$ mm, so a beam with cross section radius equal to 12 mm practically covers the entire area of the input aperture of the CPC). At each radius at input the intensity profile at output has been recorded. The optical simulations have been made by adopting an input flux proportional to the input area, maintaining in this way constant the input irradiance.

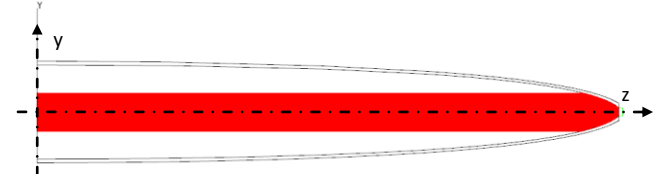


Figure 13. Irradiation of the 3D-CPC (with $R_w=1.0$) by a parallel beam of 5 mm cross section radius, incident at $\theta_{in} = 0^\circ$

Fig. 13 shows an example of these simulations, with the CPC ($R_w=1.0$) irradiated by a parallel beam with 5 mm cross section radius and incident at $\theta = 0^\circ$. The output of the CPC is closed by an ideal receiver which collects all the input rays. The eleven intensity profiles at output, obtained by simulation with TracePro[®], are shown all together in Fig. 14.

In Fig. 14 we have highlighted in bold four profiles which correspond to the full development of the five main peaks. From Fig. 15 we can see that the central peak P_I is practically absent at $r \leq 4$ mm and is almost mature at $r = 5$ mm (red profile); peak P_{II} appears at $R = 3$ mm, grows from 3 to 8 mm and is completely developed at $r = 9$ mm (green profile); peak P_{III} and P_{IV} appear at $r = 10$ mm and are completely developed at $r = 11$ mm (orange profile); peak P_V finally appears at $r = 11$ mm and is completely developed at $r = 12$ mm (blue profile). We incidentally see that the most peripheral rays at the output aperture (peak P_V) are produced by the most peripheral rays at the input aperture ($r = 11-12$ mm). We call these last rays the “skiing rays”, as they cross the CPC grazing its internal surface, making in this way several reflections (at least seven, as shown in Figs. 11 and 12) before reaching the receiver.

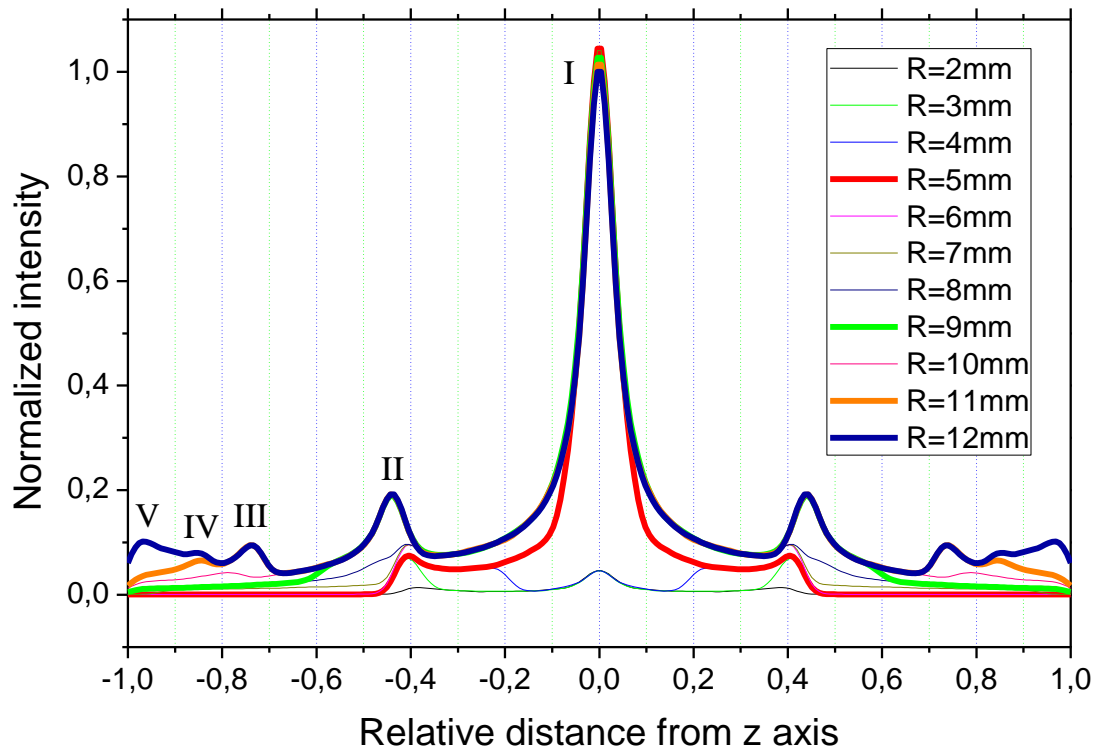


Figure 14. Intensity profiles of the flux at output of the 3D-CPC ($R_w = 1.0$), irradiated by a collimated beam parallel to the optical axis, whose cross section radius R is varied from 2 mm to 12 mm with 1 mm steps

To further analyze the evolution of the peaks as function of the cross section radius of the incident beam, we have adopted another irradiation scheme in which the parallel beam has a cross section with annular shape. The inner and outer radius of each annulus have been chosen in order to include the rays which contribute to the formation of one of the five peaks indicated in Fig. 14. Fig. 15 shows the input aperture with the scheme of the four annuli of irradiation which produce the development of the five main peaks of the flux profile at the output of the CPC: $R = 4\div 5$ mm, $8\div 9$ mm, $10\div 11$ mm and $11\div 12$ mm. Fig. 16 shows the result of four irradiation simulations, that is the intensity profiles obtained by using the four pairs of radius values for the annulus: $4\div 5$ mm (a); $8\div 9$ mm (b); $10\div 11$ mm (c); $11\div 12$ mm (d). From Fig. 16a we see that the annulus (4-5 mm) forms the peak P_I which appears a singlet; the annulus (8-9 mm) forms the peak P_{II} , but the hump on its shoulder (see Fig. 16b) betrays the presence of another small peak close to P_{II} .

The annulus (10-11 mm) forms both peaks P_{III} and P_{IV} (see Fig. 16c, black line), but, selecting a thinner annulus (10-10.5 mm) we see that P_{III} forms here, whereas P_{IV} forms in the (10.5-11 mm) annulus; finally, the annulus (d) (11-12

mm) forms the satellite peak IV, a singlet.

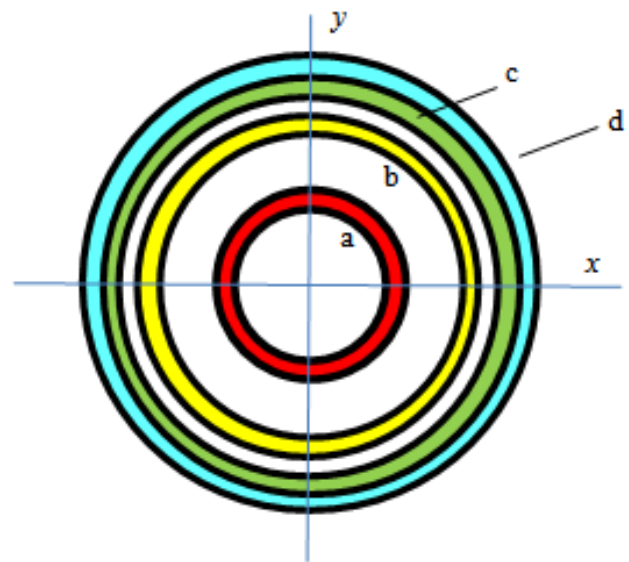
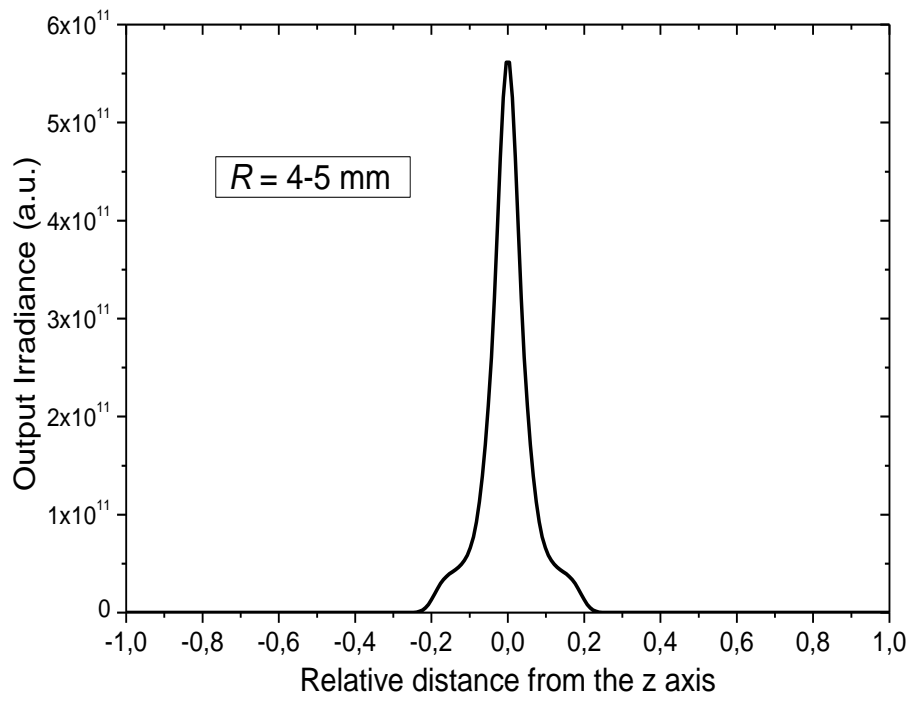
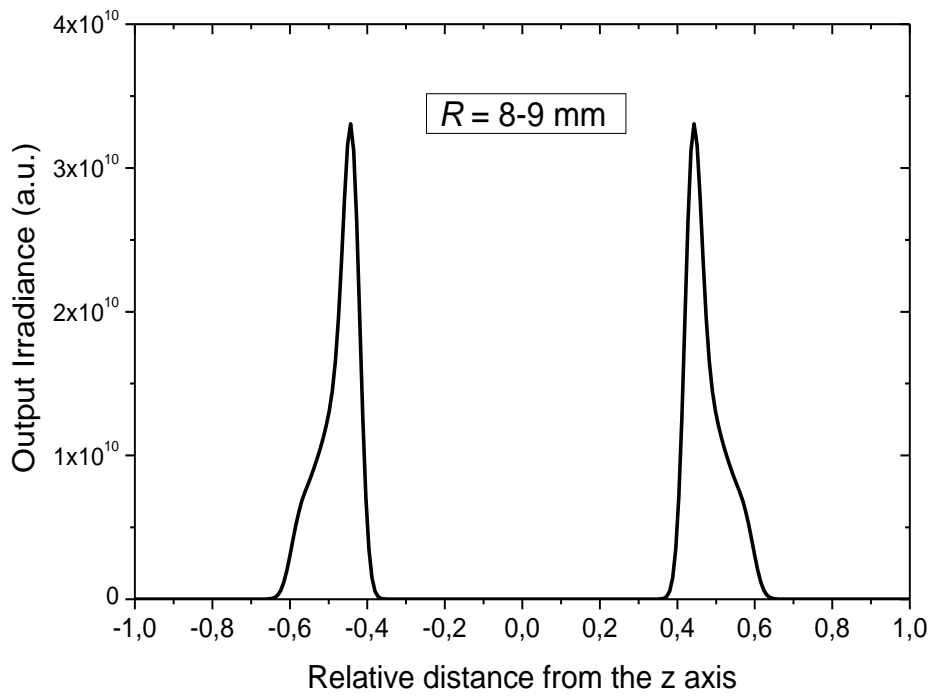


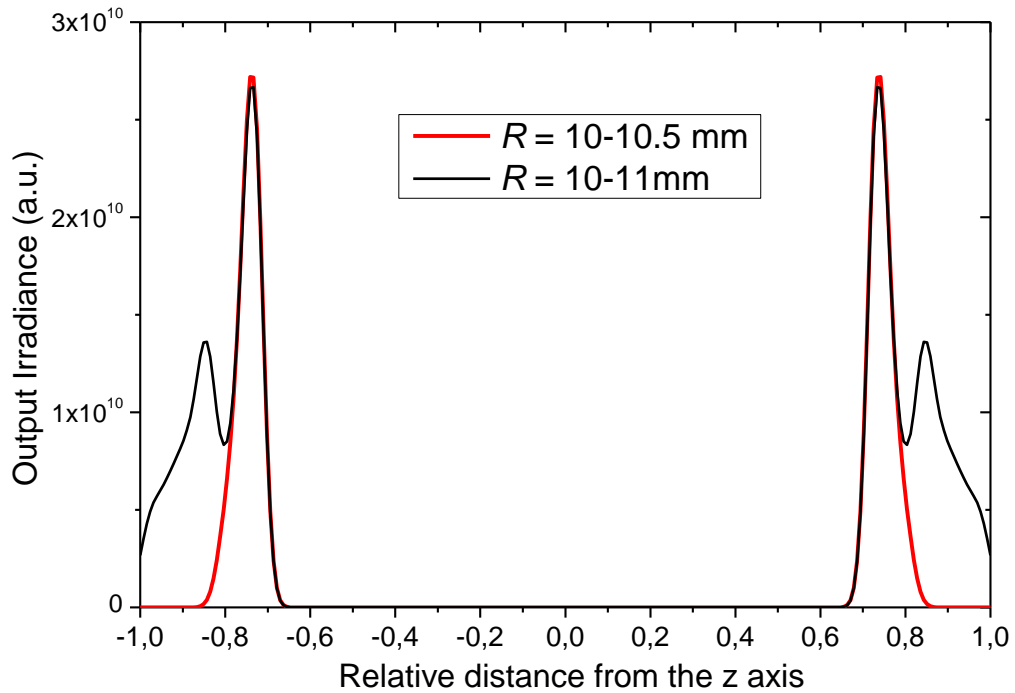
Figure 15. Scheme of the four annuli at the input aperture which generate the four main peaks on the flux profile at output of the CPC. (a) $R = 4\div 5$ mm; (b) $R = 8\div 9$ mm; (c) $R = 10\div 11$ mm; (d) $R = 11\div 12$ mm



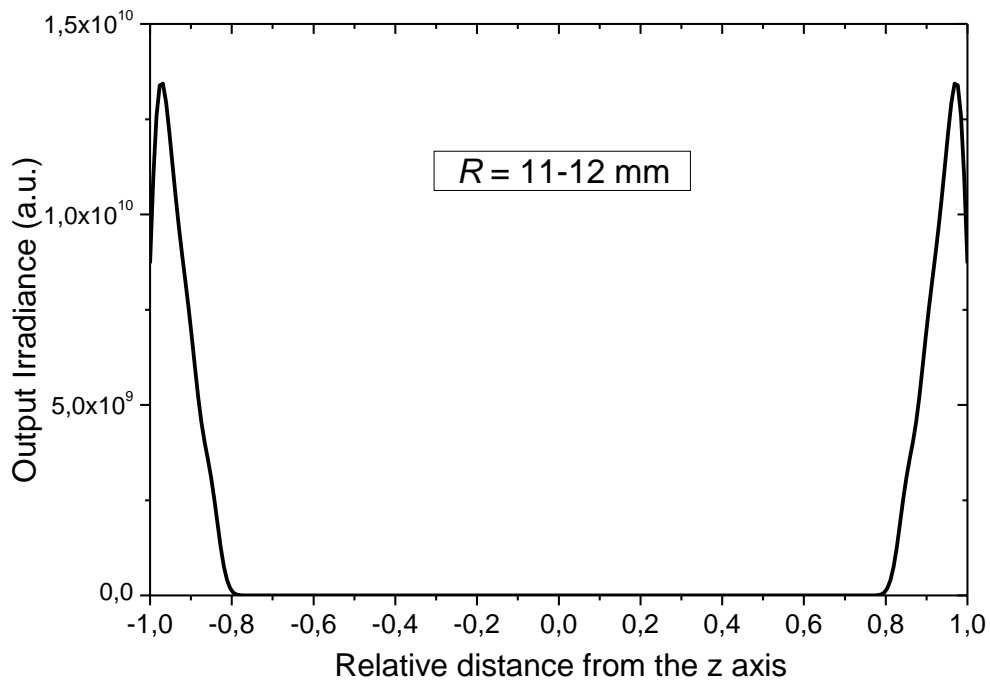
a)



b)



c)



d)

Figure 16. Radial density profiles of the output flux after irradiation of the CPC by an annulus shape with radii: 4-5mm (a), 8-9mm (b), 10-11mm (c) and 11-12mm (d)

3.6. Angular Divergence of the Transmitted Rays

The study of the angular divergence of rays at output of the CPC is important to optimize the absorption properties of the receiver. In the practical use of a PV solar concentrator, in fact, the receiver is not an ideal absorber, but a solar cell with specific reflectance properties which affect its light

absorption capabilities in relation to the divergence of the incoming rays[28]. The flux absorbed by the solar cell can be expressed as:

$$\Phi_{abs} \approx 2\pi \cdot A_{out} \cdot \int_0^{\pi/2} d\theta \cdot \sin \theta \cdot \cos \theta \cdot L_{\tau}(\theta) \cdot (1 - R(\theta)) \quad (30)$$

where A_{out} is the area of the cell, $R(\theta_m)$ is the

angle-resolved reflectance and $L_{\tau}(\theta_{in})$ is the radiance of light transmitted by the CPC (here the radiance is not function of the azimuthal angle φ because the input beam is aligned along the z axis, then the system “input beam + CPC” is rotationally symmetric).

In Eq. (30) the reflectance is considered invariant respect to the azimuthal angle; this approximation being valid for most of the commercial photovoltaic receivers. In general, however, $R(\theta_{in})$ grows with θ_{in} [18], then it is desirable that $L(\theta_{in})$ is not too high for high θ_{in} values.

To check the angular distribution of radiance of light at the CPC receiver, we have irradiated the ideal CPC ($R_w=1.0$) by a collimated beam parallel to the optical axis, and the output flux has been collected by a big hemispherical absorber (radius of 1000 mm) centered on the receiver (see Fig. 17). The rotationally symmetric map of the output flux and the corresponding radial profile are shown in Fig. 18.

The map of Fig. 18a is the flux of the screen projected on a plane orthogonal to the optical axis and $I_{pro}(\theta_{out})$ is the corresponding radial profile, where $\theta_{out} = \sin^{-1}(|x|/1000)$.

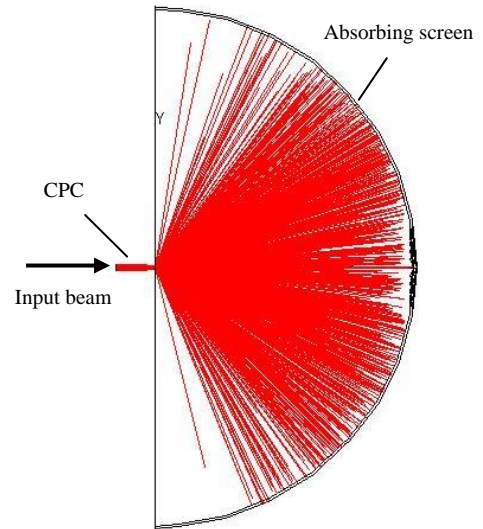


Figure 17. Scheme of the 3D-CPC irradiated by a parallel beam incident at $\theta_{in} = 0^\circ$. The output flux is collected by a hemispherical screen, with ideal absorptance

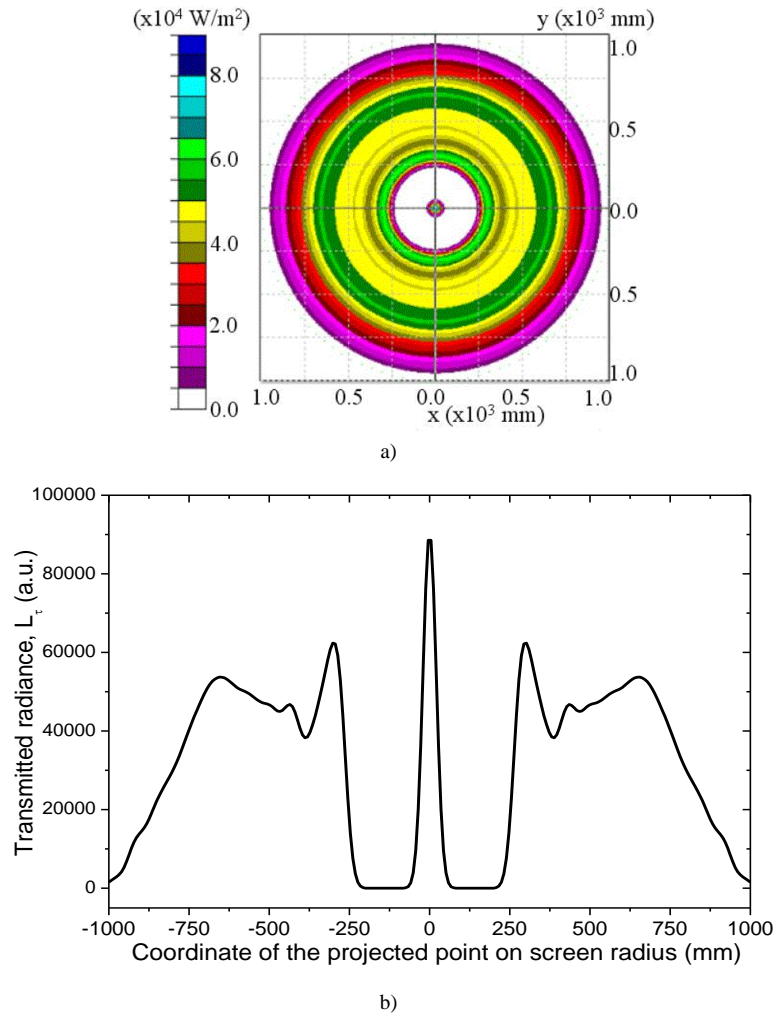


Figure 18. Map (a) and corresponding radial profile (b) of the output flux density on the hemispherical screen, projected over a plane orthogonal to the optical axis

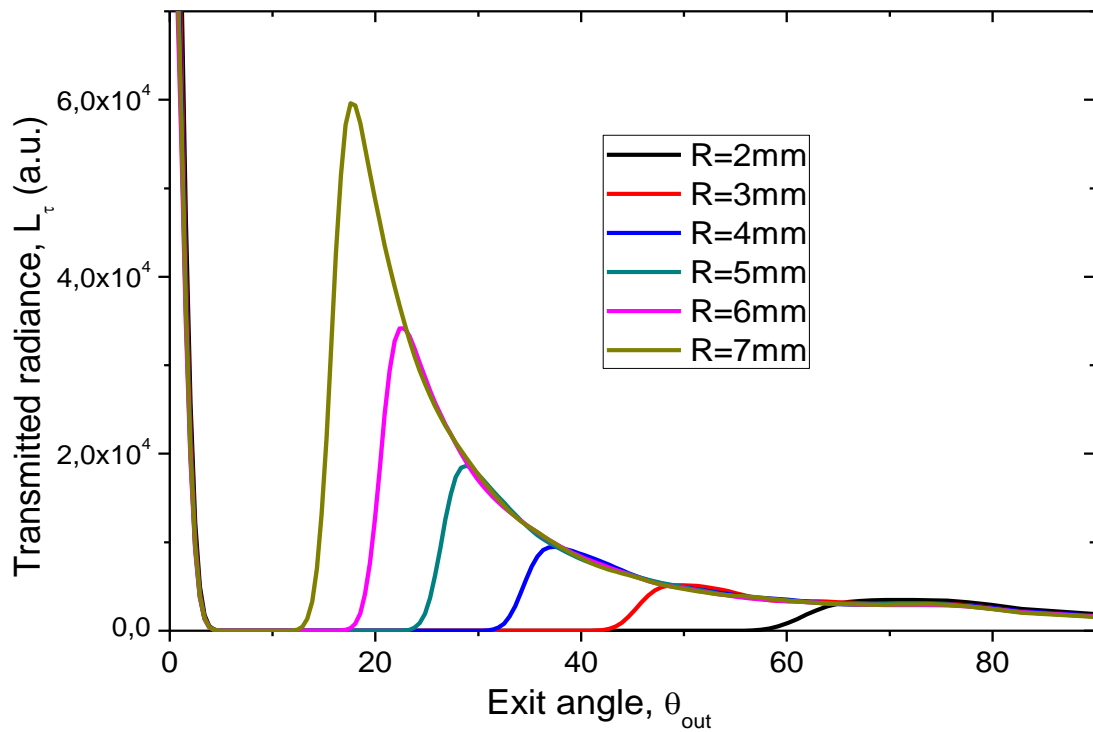


Figure 19. Radiance profiles of the flux transmitted to the output of the CPC, when the CPC is irradiated with a parallel beam with increasing cross section radius, from 2 mm to 7 mm with 1 mm steps

If $I(\theta_{out})$ is the irradiance on the screen surface, then we have: $I(\theta_{out}) = I_{pro}(\theta_{out}) \cdot \cos \theta_{out}$ and the radiance $L(\theta_{out})$ becomes:

$$L(\theta_{out}) = \frac{R^2}{A_{out} \cdot \cos \theta_{out}} \cdot I(\theta_{out}) = \frac{R^2}{A_{out}} \cdot I_{pro}(\theta_{out}) \quad (31)$$

where A_{out} is the output area of the CPC and R is the screen radius.

From Eq. (31) we see that profile of $I_{pro}(\theta_{out})$, apart from a dimensional constant factor, is the same of the radiance $L(\theta_{out})$, then the flux map of Fig. 18 is qualitatively the map of radiance. The profile of $L(\theta_{out})$ is worth of being analyzed in detail. First of all we see a central peak due to the rays which travel close to the optical axis and cross undisturbed the CPC. This bundle of rays obviously has a cross section radius equal to that of the outlet opening, $a' = 1,052$ mm. It follows a “dead” angular interval ($\theta_{out} \leq \approx 15^\circ$) with no rays, and soon after a large band that extends significantly up to about 90° (at 90° the projected point is at 1000 mm in Fig. 18b). To study the origin of this band, we proceed with the same method adopted in paragraph 3.5 to study the evolution of the output flux on the receiver. The cross section radius R of the input beam is varied from 2 mm to 12 mm with different step values and the corresponding radiance profiles are recorded.

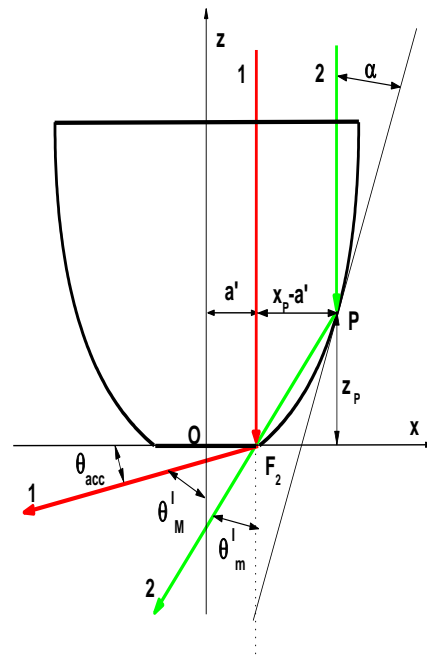


Figure 20. Scheme of the CPC irradiated by two parallel rays in the growth cycle I. The first ray (1) impinges on the point F_2 and is reflected by θ_M^I , the second (2) impinges on the point P, passes close to the point F_2 and finally exit at angle θ_m^I . Rays 1 and 2 are the extreme rays of the radiance band I

When we superimpose the different curves of radiance, we note a striking regularity in the “growth” of its profile. We identify different growth cycles of the radiance profile. In the first growth cycle (cycle I), the profile changes in a regular way from 2 to 7 mm (Fig. 19). It is characterized by rays whose angular divergence progressively decreases at increasing the radius R . Starting with small R values, indeed, the rays impact on the final portion of the CPC surface, the most inclined one (see Fig. 2), and so they undergo a large deflection. Increasing R , the incident rays move away from the optical axis and are deflected progressively less at the output.

For $R \approx 7$ mm the output rays reach the minimum divergence angle of $\approx 15^\circ$, at the left edge of the band of Fig. 19, after which a new reflection is added. This is illustrated in detail in Fig. 20. Ray 1, one extreme ray of growth cycle I, is reflected on point F_2 and exits at angle $\theta_M^I = 90^\circ - \theta_{acc} = 85^\circ$ (refer to Fig. 2 to see that beam 1, inclined of θ_{acc} , is reflected by 90° ; then a parallel beam will be reflected by $90^\circ - \theta_{acc}$). Ray 2, the other extreme ray of growth cycle I, is reflected on point P, passes close to the point F_2 and finally exit at angle θ_m^I .

To compute the angle θ_m^I , we refer to Fig. 20, where it is drawn the tangent to the CPC on point P, making the angle α with the optical axis. Considering that $\theta_m^I = 2\alpha$, we can

write down the following equation system:

$$\begin{aligned} \tan \theta_m^I &= \frac{x_P - a'}{z_P} \\ \left(\frac{dz}{dx}\right)_P &= \tan\left(\frac{\pi}{2} - \frac{\theta_m^I}{2}\right) \end{aligned} \quad (32)$$

The system (32) is solved by using the function $z(x)$ given by Eq. (6) and its derivative given by Eq. (13). The system (32) gives as solution the output angle θ_m^I and the coordinate (x_P, z_P) of the point P.

The further increase of R showed a second growth cycle (cycle II) in the $R \approx 7$ -9.7 mm interval (see Fig. 21). In this R interval, the radiance profile grows in a smaller angular interval respect to the cycle I. It involves, in fact, all the rays that make two reflections on one side of the CPC profile. The extreme rays of this II cycle are the ray 2 of Fig. 20 as soon as it is slightly moved on the right to touch the F_2 point, and a third ray which passes close to point F_2 after two reflections. It is clear, after looking at Fig. 20, that these rays, which are the extreme rays of the growth cycle II, are less divergent of the corresponding extreme rays of the growth cycle I. This is why the angular range of cycle II is comprised within that of cycle I. Continuing to increase R , we find other growth cycles of the radiance profile, each growth cycle overlapping the previous one and forming at the end the large band of Fig. 18.

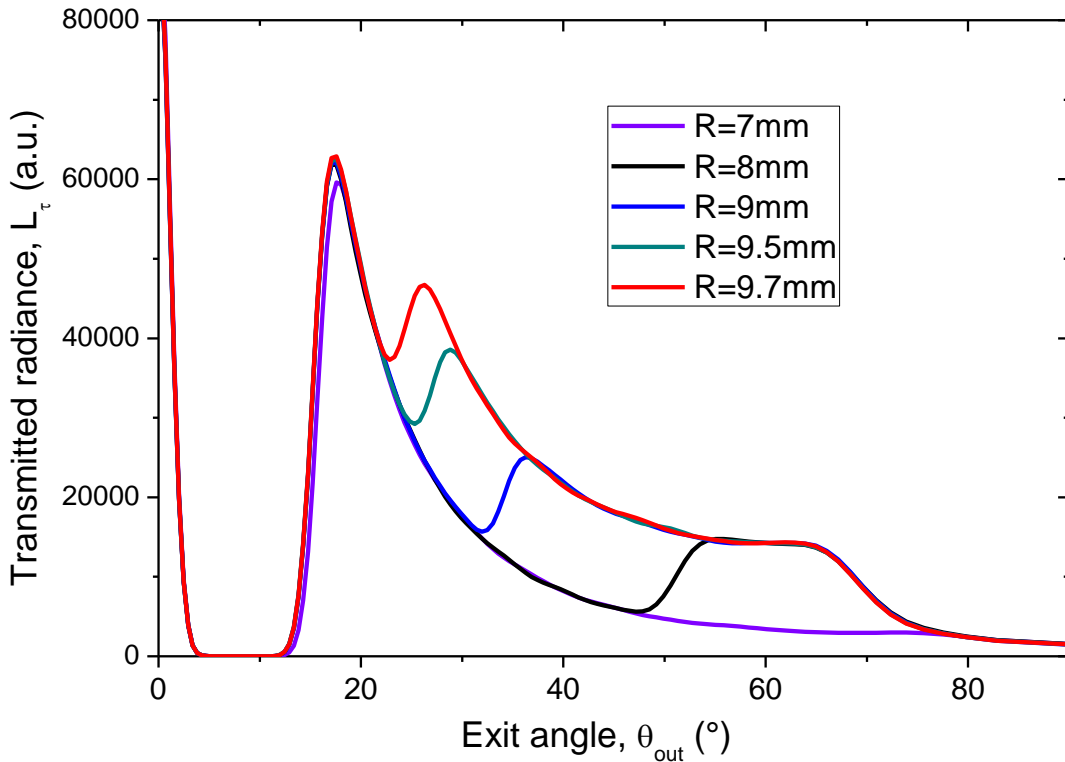


Figure 21. Radiance profiles of the flux transmitted to the output of the CPC, when the CPC is irradiated with a parallel beam with increasing cross section radius, from 7 mm to 9.7 mm

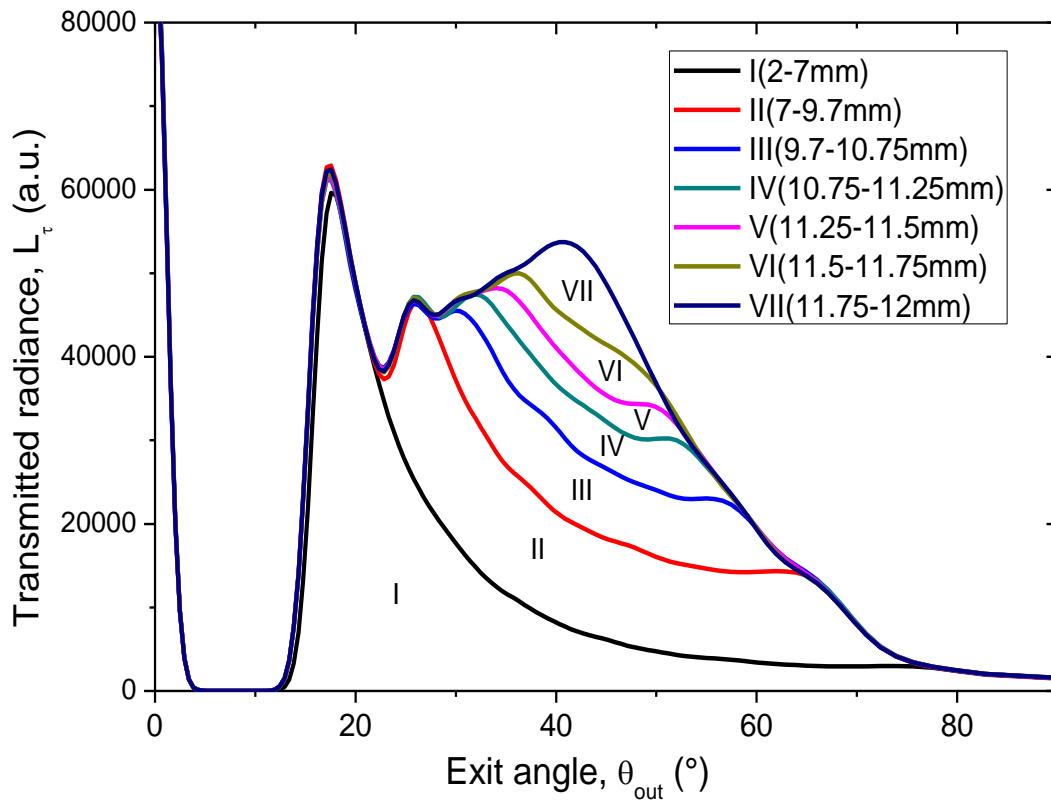


Figure 22. Radiance profiles of the different cycles of radiance growing. Each cycle is characterized by a well defined interval of r values, as indicated in the figure panel. Only seven cycles were identified, even if more others are contained in cycle VII

We point out that the number of the cycle corresponds to the number of reflections made by the rays of that cycle; the rays are reflected always on the same side of the CPC, indeed, whatever the number of reflections made, any ray is always contained in the same meridian plane of the CPC.

Fig. 22 summarizes the simulation results. The growing up of the radiance profile represented in Fig. 22 is just an approximation; we have seen in fact that the cycles after the VI one become more and more thinner and they probably give rise to an infinite succession. In effect, a parallel ray entering just at the edge of the input aperture, should make, in principle, infinite reflections, that is its path should follow exactly the CPC profile; from this the term “skiing ray” coined for this type of ray in Section 3.5. We have grouped all the cycles after the VI one in the cycle VII, which complete the profile of the band shown in Fig. 18.

Fig. 22 shows that the radiance profile, apart the “dead” interval, ending at $\theta_m^I = 15.5^\circ$ (this value corresponds to the half eight of the band I in Fig. 22), extends significantly only up to about 70° . This angle is the maximum angle of incidence of rays on the receiver, the solar cell. Although high, this angle is not too high to significantly affect the collection properties of a solar cell. As it has been shown in a previous work[28], in fact, the absorption properties of most of the commercial solar cells are sufficiently good in the $0-70^\circ$ interval.

The values of the extreme angles θ_M and θ_m for each growth cycle, from I to VI, have been also obtained by

raytracing a single ray parallel to the optical axis and looking at its path as schematized in Fig. 20. They are reported in Table 3. The column of R (mm) displays the two extreme values R_M and R_m of distance of the ray from the optical axis, corresponding to the two extreme values of the angle: θ_M and θ_m . The values of R_M , R_m , θ_M and θ_m calculated for the single ray slightly differ from those obtained qualitatively by looking at the modifications of the radiance profile following a try and error procedure.

Table 3. Accurate values of maximum and minimum divergence angle of single ray in each growth cycle, from I to VI, together with the corresponding distance of the input ray from the optical axis

Cycle	R_M (mm)	R_m (mm)	θ_M ($^\circ$)	θ_m ($^\circ$)
I	1.0523	7.1194	84.96	15.53
II	7.1195	9.719	69.21	24.26
III	9.720	10.740	60.36	29.06
IV	10.75	11.22	55.42	31.92
V	11.23	11.48	52.41	33.66
VI	11.49	11.63	50.05	35.27

4. Analysis of the Reflected Flux

4.1. Optical Reflection Efficiency

The study of the angular divergence of back reflected rays from input aperture has not a practical relevance as it has in the case of the transmitted rays, but it is a useful exercise to

apply well known concepts of the theory of solar concentrators. Let us consider at first the total reflected flux:

$$\begin{aligned}\Phi_{\rho} &= \Phi_{in} - \Phi_{\alpha} - \Phi_{\tau} = \Phi_{in} \cdot \eta_{\rho}(R_w, \theta_{in}) = \dots \\ &\dots = \Phi_{in} \cdot [1 - \eta_{\tau}(R_w, \theta_{in}) - \eta_{\alpha}(R_w, \theta_{in})]\end{aligned}\quad (33)$$

where $\eta_{\rho}(R_w, \theta_{in})$ and $\eta_{\alpha}(R_w, \theta_{in})$ are the reflection and absorption efficiencies, respectively, and the other quantities are defined in section 3.3. The total reflected flux can be expressed as function of the radiance $L_{\rho}(R_w, \theta_{in}, \theta_{out}, \phi_{out})$ of reflected light:

$$\begin{aligned}\Phi_{\rho}(R_w, \theta_{in}) &= \dots \\ &= A_{in} \cdot \int_0^{2\pi} d\phi_{out} \int_0^{\pi/2} d\theta_{out} \cdot \sin \theta_{out} \cdot \cos \theta_{out} \cdot L_{\rho}(R_w, \theta_{in}, \theta_{out}, \phi_{out})\end{aligned}\quad (34)$$

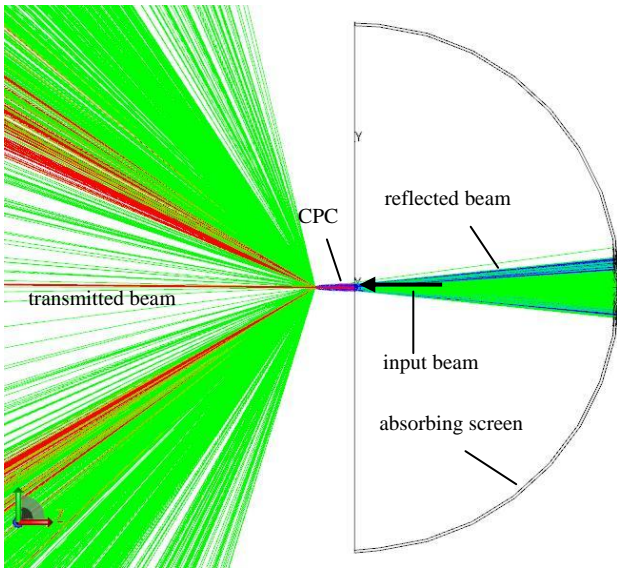


Figure 23. Scheme of the 3D-CPC irradiated by a parallel beam incident at variable angle θ_{in} . The reflected flux is measured by an absorbing hemispherical screen. The CPC of the figure is not ideal ($R_w=0.8$), as consequence, the incident rays (red color) are attenuated after reflection (green and blue color). The output of the CPC has been left open, so the transmitted rays are visible. Most of the transmitted rays are attenuated (green color); the red beam on the z axis is made of rays crossing undisturbed the CPC

In order to simulate the reflection properties of the CPC, we have adopted a scheme similar to that used to measure the transmitted light (see Fig. 23). The input aperture of the CPC is irradiated in direct mode by a collimated beam of constant flux and inclined at different angles θ_{in} , and the reflected rays are collected by a large hemispherical screen (of 1000 mm radius) with ideal absorbance. The CPC protrudes out of the screen and the center of input aperture meets that of the screen. The input collimated beam is not visible in Fig. 23,

because it is applied just at the input aperture of the CPC, but is schematized as an arrow.

The optical reflection efficiency is defined as the ratio of the output to the input flux:

$$\eta_{\rho}(R_w, \theta_{in}) = \frac{\Phi_{\rho}(R_w, \theta_{in})}{\Phi_{in}}\quad (35)$$

Only for $R_w = 1.0$ this ratio is equal to the ratio between the number of output to input rays, because of the absence of optical loss inside the CPC. Fig. 24 shows the curve of reflection efficiency calculated for $R_w = 1.0, 0.9$ and 0.8 .

We note that the reflection efficiency is low below the acceptance angle, as most of rays are transmitted; then it increases, in correspondence of θ_{acc} , in a different way depending on R_w . For $R_w = 1.0$ the efficiency is unitary, that is all the non transmitted rays are reflected without optical loss. For $R_w < 1$, instead, we have a fall of efficiency, higher for lower R_w values, which increases in a fairly linear way with the increase of the angle of incidence. This progressive fall of efficiency is due to the loss of beam energy for absorption internal to the CPC, which grows because the average number of reflections grows with θ_{in} . The dependence of the number of reflections of rays as function of the incidence angle will be the argument of a forthcoming section.

Fig. 25 shows the number of rays outgoing from the input aperture of the CPC after back reflection, obtained by the simulations performed with three values of R_w . The number of back reflected rays is low below the acceptance angle, as most of rays are transmitted, then we have a step-like transition to high values in correspondence of θ_{acc} . For $\theta_{in} > \theta_{acc}$ and $R_w = 1.0$ the number of reflected rays is equal to the number of input rays, whereas, for $R_w < 1.0$, this number decreases because some of rays, those undergoing the greatest number of reflections, have insufficient power to be counted as output beams.

This effect, of course, is more pronounced for smaller R_w values ($R_w = 0.8$). In section 4.3, the number of back reflected rays, together with the reflection efficiency of Eq. (35) will be used to derive the average number of reflections internal to the CPC of the back reflected rays.

4.2. Angular Divergence of the Reflected Rays

In order to simplify the discussion, we confine our study of the angular divergence of reflected rays to the ideal CPC ($R_w = 1$). We have:

$$\Phi_{\rho} = \Phi_{in} - \Phi_{\tau} = \Phi_{in} \cdot [1 - \eta_{\tau}(\theta_{in})] = \Phi_{in} \cdot \eta_{\rho}(\theta_{in})\quad (36)$$

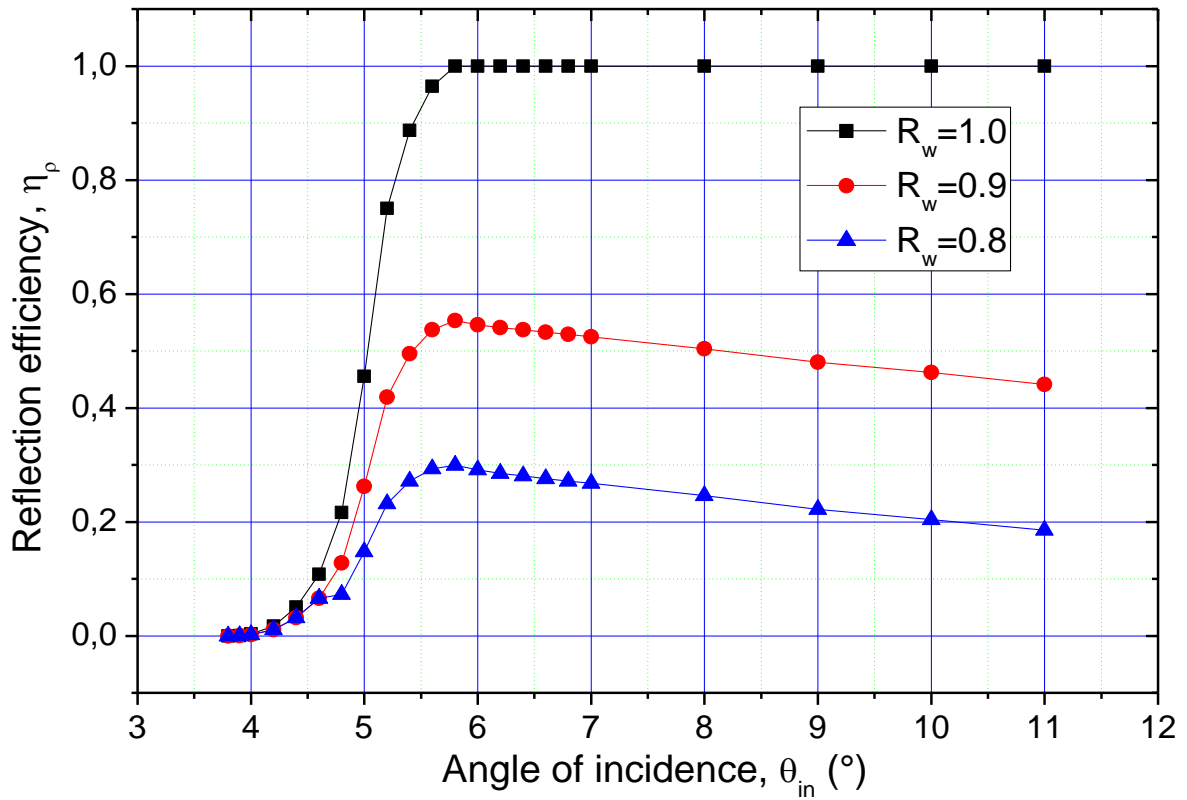


Figure 24. Optical reflection efficiency $\eta_p(R_w, \theta_{in})$ of the 3D-CPC calculated for three wall reflectivities: $R_w = 1.0, 0.9$ and 0.8

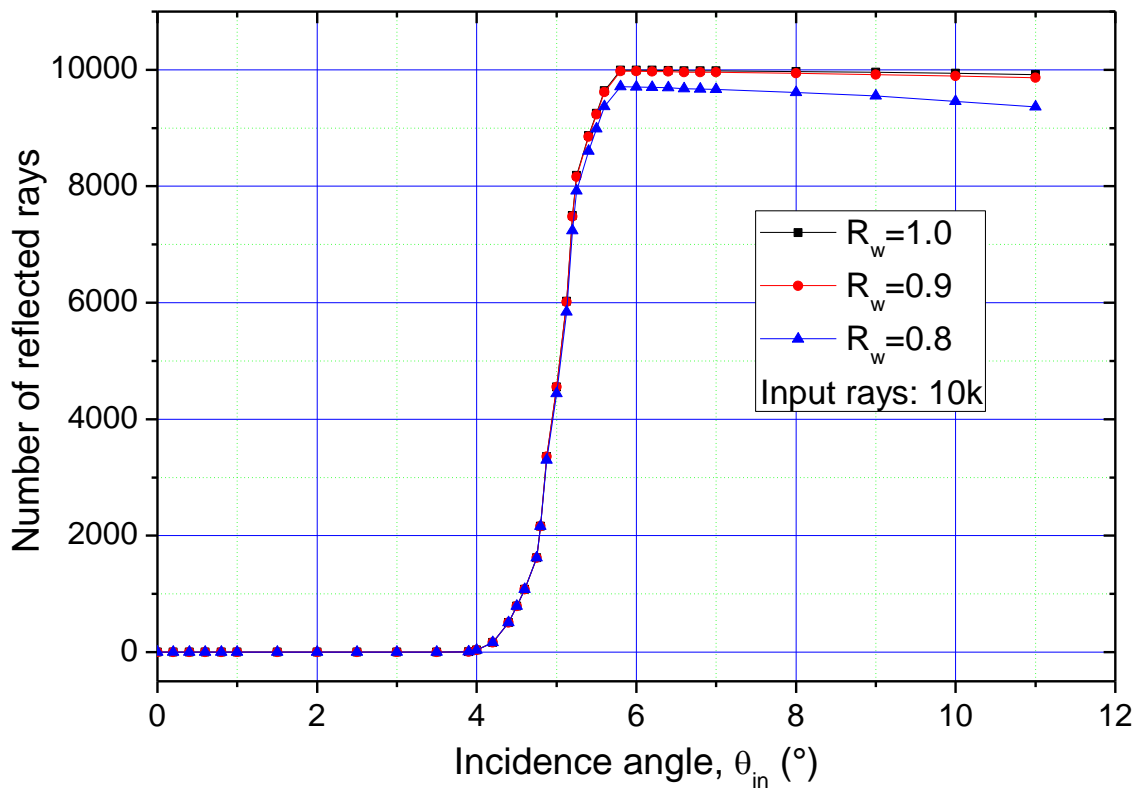


Figure 25. Number of output rays back reflected by the CPC, as function of the incidence angle of the collimated beam, calculated for three wall reflectivities: $R_w = 1.0, 0.9$ and 0.8

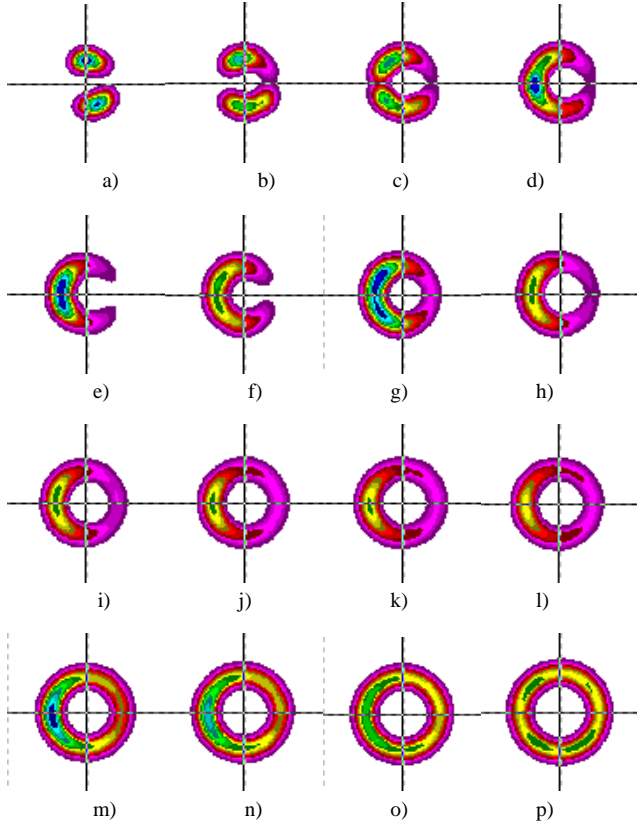


Figure 26. Maps of radiance of the reflected light, measured as function of the angle of incidence θ_{in} of the collimated beam at input aperture, for $R_w = 1.0$. Incidence angles: 4.0 °(a); 4.2 °(b); 4.4 °(c); 4.6 °(d); 4.8 °(e); 5.0 °(f); 5.2 °(g); 5.4 °(h); 5.6 °(i); 5.8 °(j); 6.0 °(k); 6.2 °(l); 6.4 °(m); 6.6 °(n); 6.8 °(o); 7.0 °(p)

The reflection efficiency becomes simply the complement to 1 of the transmission efficiency. As already seen discussing the transmitted light, when the flux exiting from the CPC is collected by the hemispherical screen, the TracePro software produces a map corresponding to the irradiance on the screen wall projected on a plane orthogonal to the z axis. Apart from a dimensional constant factor, this map is equivalent to that of the radiance of light back reflected by the input aperture, as it has been demonstrated in Eq. (31). Some maps obtained at different incidence angles of the collimated beam respect to the z axis are shown in Fig. 26; they reveal an asymmetry along the x axis (the horizontal axis in the figure) because the incidence plane of the beam is the x/z plane.

We found that $\theta_{in} = 3.9^\circ$ was the minimum angle for detecting reflected rays. We observe a strong asymmetry of the maps for $\theta_{in} \approx \theta_{acc}$ (5°), which reduces at increasing θ_{in} . For θ_{in} values well higher than the acceptance angle, the asymmetry seems to disappear, that means that the reflected

rays tend to forget the information of direction of the incident rays. This is a consequence of an increase of the number of reflections when the incident angle is increased, as it will be illustrated in section 4.3.

For the moment, we analyze the “average” angular divergence of the reflected rays, being the average made on the azimuthal angle of the “incident” plane. Here we look for a correlation between the “average” angular divergence of reflected rays and the angular divergence of input rays. To do this, all the maps of Fig. 26 were rotationally symmetrized and their radial profiles plotted as function of the exit angle (see Fig. 27).

We observe that the radiance increases, reaches a maximum at $\theta_{in} \approx 5.8^\circ$ and then decreases. The increase is due to the decrease of number of transmitted rays, which, from the point of view of the reflected ones, are equivalent to an optical loss. At $\theta_{in} \geq 5.8^\circ$ all the rays are reflected, as it can be seen in Fig. 24, and, as the input flux is kept constant, the reflected flux must be constant as well:

$$\begin{aligned} \Phi_\rho(\theta_{in} \geq 5.8^\circ) &= \dots \\ &= A_{in} \cdot 2\pi \cdot \int_0^{\pi/2} d\theta_{out} \cdot \sin \theta_{out} \cdot \cos \theta_{out} \cdot L_\rho(\theta_{out}) = \text{const} \quad (37) \end{aligned}$$

The simulations show that the width at half maximum of the radiance peak results strictly independent from θ_{in} : $\Delta L_\rho(\theta_{in}) = 2.93 \pm 0.04^\circ$; this result is not explained. Consequence of the invariance of $\Delta L_\rho(\theta_{in})$ is that, to have a constant integral in Eq. (37), the maximum of radiance peak must follow this trend:

$$L_\rho^{\max}(\theta_{out}) = \text{const} \cdot \frac{1}{(\sin \theta_{out} \cdot \cos \theta_{out})} \quad (38)$$

The dashed curve in Fig. 27 is just a function of the type $(\sin \theta_{out} \cdot \cos \theta_{out})^{-1}$ and it perfectly matches all the peaks of radiance for $\theta_{in} \geq 5.8^\circ$. By plotting the angle corresponding to the peak of each radiance profile (the average reflecting angle) versus the incident angle, we obtain the graph of Fig. 28.

The data of $\bar{\theta}_{out}$ vs. θ_{in} , taken $\theta_{in} > \theta_{acc}$ show a linear trend: $\bar{\theta}_{out} = -0.452 + 1.025 \cdot \theta_{in}$. Apart from small differences, not explained, we can affirm that $\bar{\theta}_{out} \approx \theta_{in}$.

This result is a direct consequence of the Liouville theorem which establishes the invariance of the “generalized étendue”, the volume occupied by the system in the phase space (see Fig. 29):

$$n^2 \cdot A \cdot \sin^2 \theta = (n')^2 \cdot A' \cdot \sin^2 \theta' = \text{const} \quad (39)$$

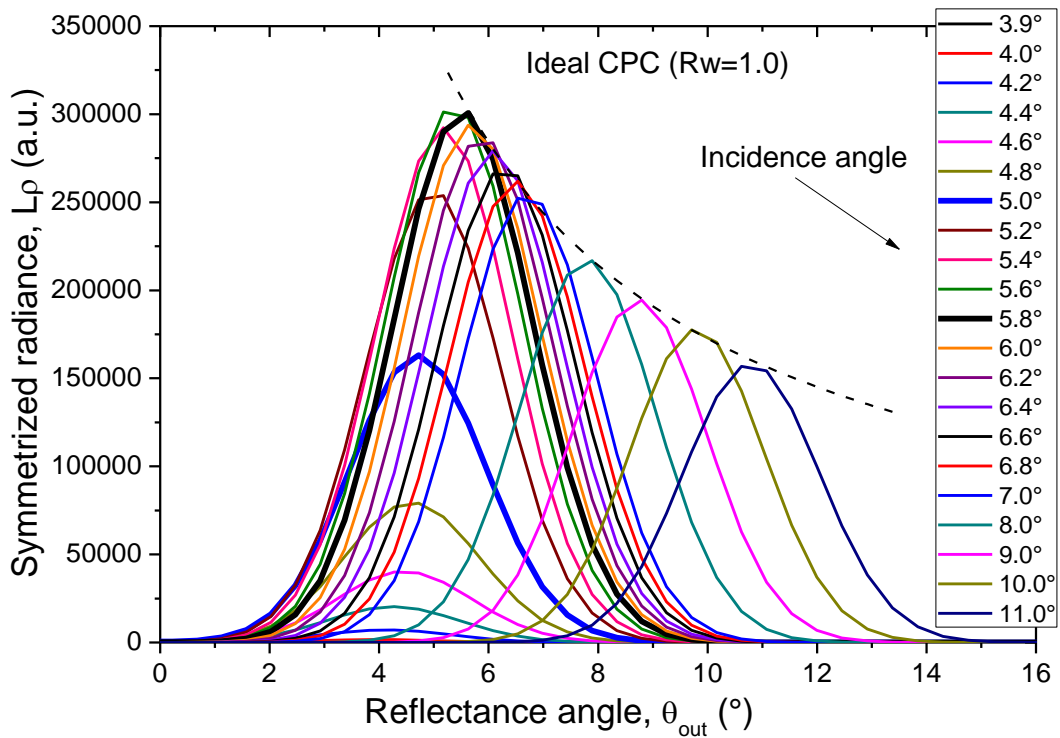


Figure 27. All the profiles of the reflection radiance obtained after rotational symmetrization of the radiance maps of Fig. 26. The blue curve of $\theta_{in}=5^\circ$ (acceptance angle) and the black curve of $\theta_{in}=5.8^\circ$ (only reflected rays) are in bold

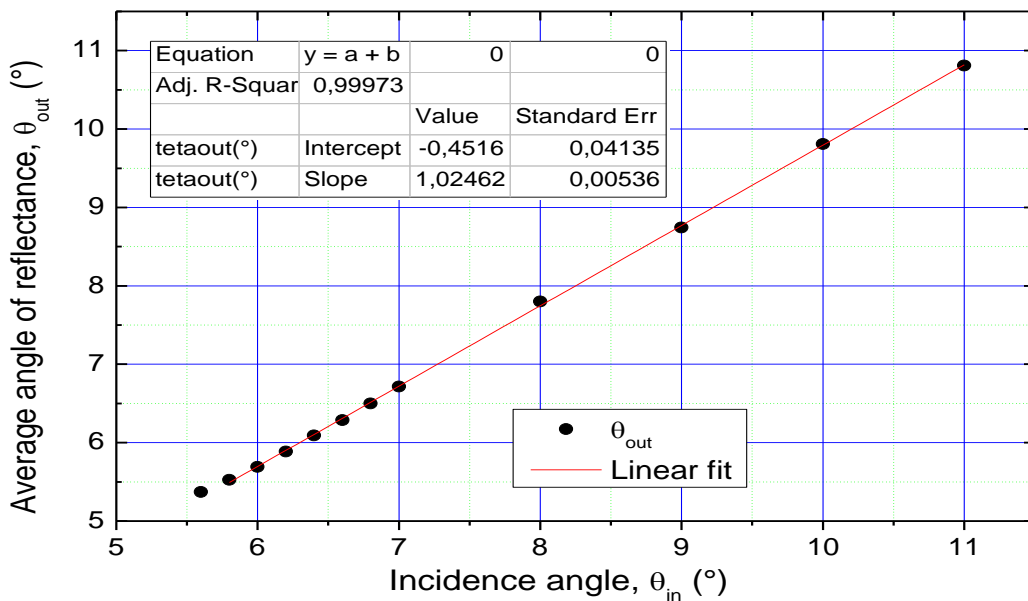


Figure 28. Average angle of reflection as function of the incidence angle of the collimated beam (dots). Linear fit of data with $\theta_{in} \geq 5.8^\circ$ (red line)

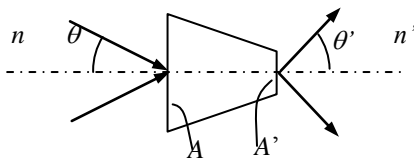


Figure 29. Scheme of a generic concentrator with the three main parameters for the input and output apertures: index of refraction, area and angular divergence

In our case the incident and reflected rays are in air ($n, n' = 1$) and cross the same port, the input aperture of area A_{in} , then we have:

$$A_{in} \cdot \sin^2 \theta_{in} = A_{in} \cdot \sin^2 \theta_{out} \Rightarrow \theta_{in} = \theta_{out} \quad (40)$$

which confirms the result of the simulations (Fig. 28). The question remains open as to why $\bar{\theta}_{out}$ is not exactly equal to θ_{in} .

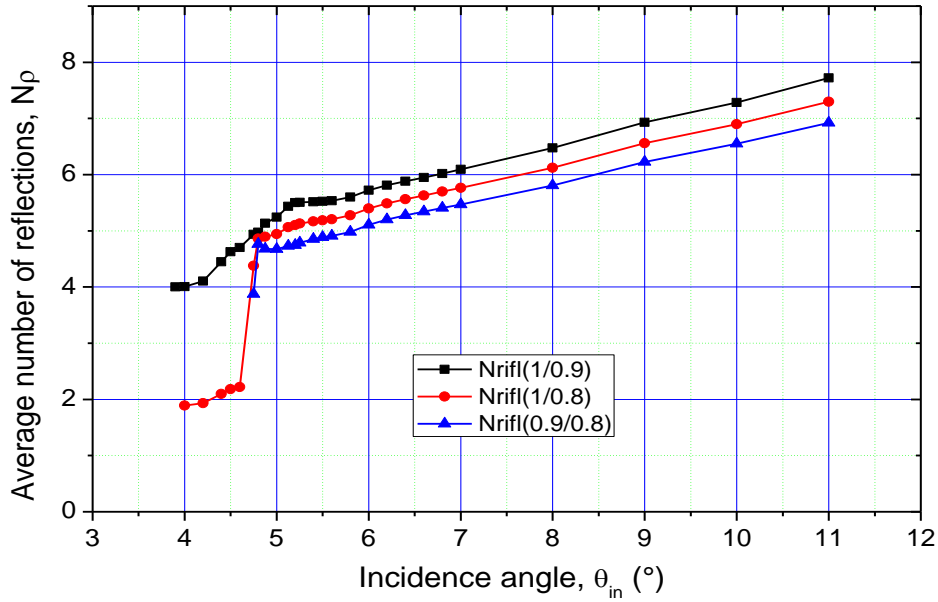


Figure 30. Average number of internal reflections of back reflected rays, simulated by applying Eq. (43) for three different pairs of values of internal wall reflectivity: $(R'_w, R''_w) = (1.0; 0.9), (1.0; 0.8), (0.9; 0.8)$

4.3. Number of Internal Reflections of the Back Reflected Rays

The reflected flux can be expressed in a way similar to that of the transmitted flux (see Eq. (19)):

$$\Phi_{\rho}(R_w, \theta_{in}) = \sum_{j=1}^{N_{in}} \phi_{in} \cdot (R_w)^{N_j(\theta_{in}, \phi_{in}, P)} = \dots \quad (41)$$

$$\dots = N_{\rho}(R_w, \theta_{in}) \cdot \phi_{in} \cdot (R_w)^{\bar{N}_{\rho}(R_w, \theta_{in})}$$

From Eq.s (35), (41) we derive the reflection efficiency:

$$\eta_{\rho}(\theta, R_w) = \frac{N_{\rho}(R_w, \theta_{in}) \cdot (R_w)^{\bar{N}_{\rho}(R_w, \theta_{in})}}{N_{in}} \quad (42)$$

If the reflection efficiency is measured for two different but closed wall reflectivities, R'_w and R''_w , we finally obtain, in analogy with the transmitted rays, the expression for the average number of internal reflections of the back reflected rays:

$$\bar{N}_{\rho}(R'_w, R''_w, \theta_{in}) \approx \frac{\log \left[\frac{\eta_{\rho}(R'_w, \theta_{in}) \cdot N_{\rho}(R''_w, \theta_{in})}{\eta_{\rho}(R''_w, \theta_{in}) \cdot N_{\rho}(R'_w, \theta_{in})} \right]}{\log \left[\frac{R'_w}{R''_w} \right]} \quad (43)$$

We use now the reflection efficiency data measured at $R_w = 1.0, 0.9$ and 0.8 (see Fig. 24), to simulate the average number of internal reflections of the back reflected rays. Fig. 30 shows the curves of $\bar{N}_{\rho}(R'_w, R''_w, \theta_{in})$ obtained applying Eq. (43) to the three pairs of reflectivity: $(1.0; 0.9)$, $(1.0, 0.8)$ and $(0.9, 0.8)$. We note that, first of all, the number of reflections slightly decreases with decreasing the average reflectivity of the pair, as it was observed for the case of transmitted rays. Moreover, we note that, for incidence

angles greater than θ_{acc} , $\bar{N}_{\rho}(R'_w, R''_w, \theta_{in})$ increases in a strictly linear way with increasing the angle of incidence θ_{in} .

The average value of $\bar{N}_{\rho}(R'_w, R''_w, \theta_{in})$, calculated for the three pairs of reflectivities shows the following dependence on θ_{in} , when $\theta_{in} \geq \theta_{acc}$:

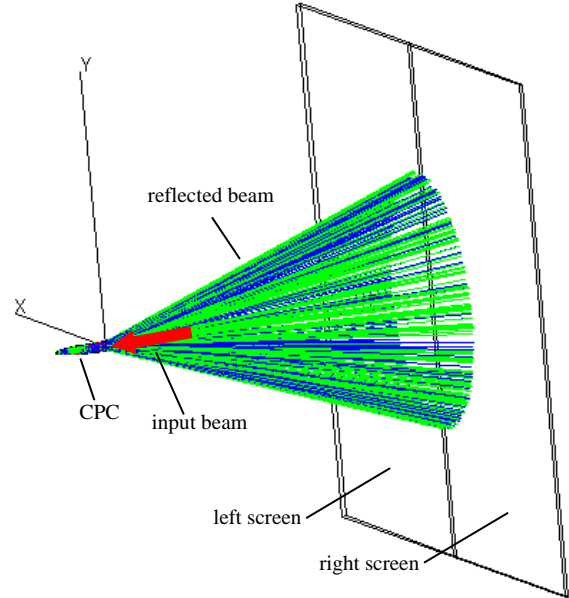


Figure 31. Scheme used to compute the asymmetry of the flux reflected by the CPC irradiated by a parallel beam. The reflected flux impinges on two planar screens, left and right in the figure, and the corresponding fluxes are separately measured. The input flux, not visible, is schematized by the red arrow. The transmitted flux has been absorbed at the exit aperture. The reflected flux is clearly distributed on the surface of a cone with aperture equal to $2 \times \theta_{in}$.

$$\bar{N}_\rho(\theta_{in}) = 3.07(\pm 0.028) + 0.386(\pm 0.0043) \cdot \theta_{in} \quad (44)$$

4.5. Symmetry of the Back Reflected Beam

As we have seen from Fig. 26, the maps of radiance of the back reflected beam show a marked asymmetry at low θ_{in} values, which gradually decreases with the increase of θ_{in} . Here we study in detail this dependence, asymmetry of the beam vs. angle of incidence, to find out if there is a sharp transition to symmetry or if the transformation of the map is gradual. To do this, we quantify the degree of symmetry of each map by separating the left from the right side, and taking the ratio between the corresponding fluxes. The degree of symmetry has been expressed as:

$$\sigma(\theta_{in}) = \frac{\Phi_L(\theta_{in})}{\Phi_R(\theta_{in})} \quad (45)$$

where $\Phi_L(\theta_{in})$ and $\Phi_R(\theta_{in})$ are the flux at left side and right side, respectively. To compute $\sigma(\theta_{in})$, we have replaced the hemispherical screen by two planar absorbing screens, one on the left side ($x > 0$) and the other on the right side ($x < 0$) (see Fig. 31). The screens are placed very far from the CPC, in order to discriminate well the rays directed towards the two directions. The left and right fluxes are simply read as total flux absorbed by each screen. The degree of symmetry, computed for the CPC with $R_w = 1.0$, is shown

in Fig. 32. The approach to symmetry does not occur through a net transition, but through an oscillation of $\sigma(\theta_{in})$, more and more attenuated, having the unit as limit. We examined high angles of incidence, much higher than those examined for the transmission of light, in order to investigate some fundamental properties of the CPC, irrespective of its application as a solar concentrator.

The simulations show that at $\theta_{in} = 60^\circ$ a degree of symmetry better than 97% is reached.

5. Analysis of the Absorbed Flux

5.1. Optical Absorption Efficiency

From the data of transmission efficiency and reflection efficiency we immediately derive the ‘‘absorption efficiency’’ by the expression[1]:

$$\eta_\alpha(\theta_{in}) = 1 - \eta_\tau(\theta_{in}) - \eta_\rho(\theta_{in}) \quad (46)$$

The absorption efficiency as function of incidence angle, calculated for three wall reflectivities: $R_w = 1.0, 0.9$ and 0.8 . is shown in Fig. 33. For $R_w = 1.0$ we have no absorption of light, $\eta_\alpha(1, \theta_{in}) = 0$, whereas, for $R_w = 0.9$ and 0.8 we have always an optical absorption inside the CPC.

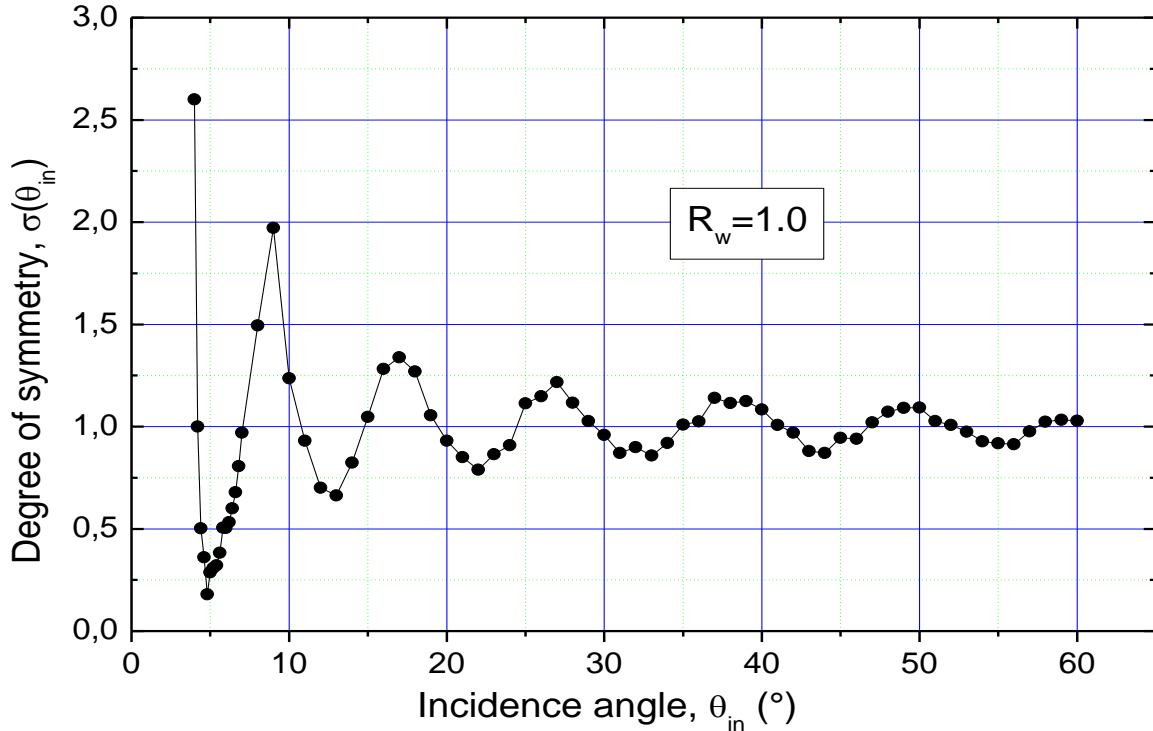


Figure 32. Degree of the symmetry, $\sigma(\theta_{in})$, of the radiance map of back reflected rays from the CPC, as function of the incidence angle θ_{in} , calculated for unitary reflectivity of the internal wall

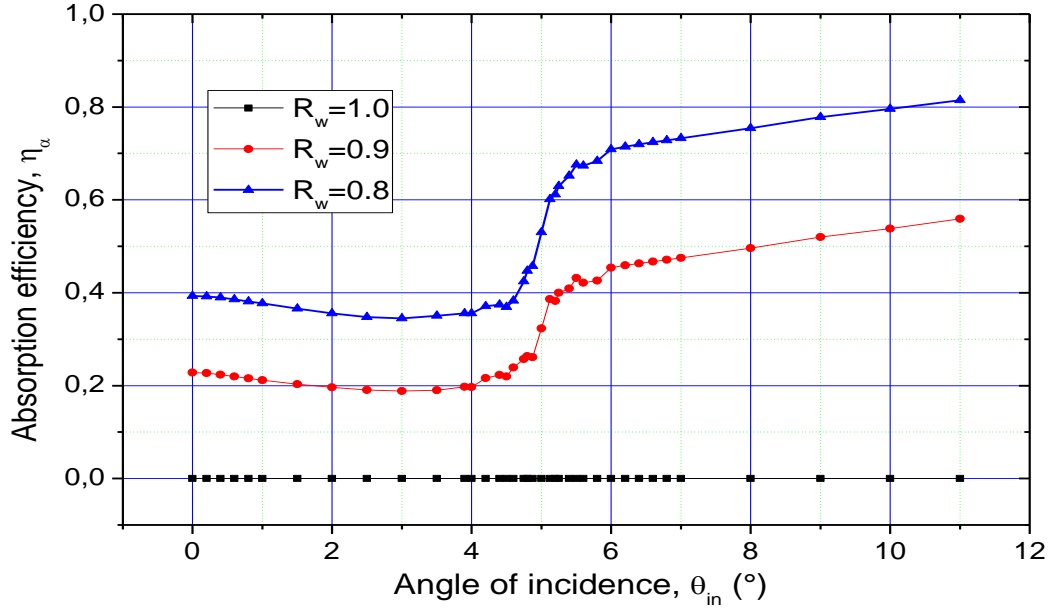


Figure 33. Absorption efficiency $\eta_\alpha(R_w, \theta_{in})$ of the 3D-CPC calculated for three wall reflectivities: $R_w = 1.0, 0.9$ and 0.8

For $\theta_{in} < \theta_{acc}$ the absorption of light is due to the internal reflections of mainly the transmitted rays, these reflections being about 2, as we see in Fig. 8. For $\theta_{in} > \theta_{acc}$, instead, the absorption of light inside the CPC is made mainly of back reflected rays, whose average number of internal reflections is higher, more than about 5, as shown in Fig. 30. As consequence, the absorption efficiency is higher at $\theta_{in} > \theta_{acc}$ respect to $\theta_{in} < \theta_{acc}$, and the final effect is a step-like transition of the $\eta_\alpha(R_w, \theta_{in})$ at $\theta_{in} = \theta_{acc}$, as shown in Fig. 33. For $\theta_{in} > \theta_{acc}$ the absorption efficiency increases linearly, as an effect of the linearly increase of number of internal reflections (Fig. 30). For $\theta_{in} < \theta_{acc}$ the absorption fractions are about 0.2 and 0.4, for $R_w = 0.9$ and 0.8 respectively, complement to one of the 0.8 and 0.6 fractions of transmittance (Fig. 5), as the reflection efficiency is very low in this angular interval (Fig. 24).

5.2. Distribution of the Absorbed Flux

Here we study how the absorbed flux is distributed inside the CPC. At this purpose a value of wall reflectivity < 1 has been selected. After each irradiation, by selecting the internal wall of the CPC, it is produced a map of the absorbed flux, projected on the x/y plane orthogonal to the optical axis z . In this way, the map is circular and of the dimension of the input aperture and the reported intensity is the projection on the x/y plane of the absorbed irradiation (in W/m^2). Some maps of the absorbed flux are shown in Fig. 34 for a wall reflectivity of $R_w = 0.9$, a typical value for realistic solar concentrators. The incidence angle of the collimated beam has been varied from 0° to 20° . The incidence plane of the beam was the x/z one and the beam was inclined towards the $x > 0$ direction (right side in Fig. 34). From Fig. 34 we can make a qualitative estimation of the areas of the internal

surface which absorb more light. The map of absorbed flux (the absorbed irradiance) is qualitatively equivalent to the map of incident flux (the incident irradiance), being the absorbed flux a fixed fraction of the incident flux, that is 10% in the actual case.

From Fig. 34 we see that, at $\theta_{in} = 0^\circ$ all the CPC surface is irradiated, but most of light is absorbed near the exit aperture; at increasing θ_{in} the flux moves towards the left side of the CPC, where is directed the input beam, but, passed the acceptance angle (5°), the flow tends to be distributed also on the right side, as a result of the multiple internal reflections undergone by the reflected rays (see Fig. 30). It is interesting to study the average distribution of the flux along the z coordinate (the optical axis). To do this, we make at first the rotational symmetry of each map of Fig. 34, then we take its radial profile plotted as function of the z coordinate, and finally the intensity profile is corrected by the $\cos\alpha$ factor, to remove the projection made by the program, where α is the angle that the tangent to the CPC profile makes with the optical axis (see Eq. (13) and Fig. 20).

$$\alpha = \frac{\pi}{2} - \arctg\left(\frac{dz}{dx}\right) = \frac{\pi}{2} + \dots \quad (47)$$

$$- \arctg\left\{ \left[\frac{e}{2\sqrt{b^2 - 4(4f \cdot x + c) \cdot \sin\theta_{acc}}} - d \right] \cdot (16f \cdot \sin\theta_{acc}) \right\}$$

The final result is the profile of the absorbed irradiance, as reported in Figs. 35 and 36, for incidence angles in the 0° – 20° interval. Fig. 35 shows the portion of the CPC near the exit aperture with some interesting features: the absorbed irradiance at $\theta_{in} < \theta_{acc}$ (5°) is not high as the flux is mainly transmitted; the irradiance makes a jump at $\theta_{in} = \theta_{acc}$ (the 5° green profile is traced bold in Fig. 35) and remains high at all angles, but tends to move towards the

center of the CPC at increasing θ_{in} .

Fig. 36 shows the entire irradiance profiles along the CPC. Apart from the central peak near $z = 0$, illustrated in Fig. 35, we note some interesting features: the absorbed irradiance grows at increasing θ_{in} , particularly at $\theta_{in} >$

θ_{acc} , but the growth is particularly evident in the portion near the entrance of the CPC, where it is forming a large band. The effect of the inclination of the input beam is ultimately to move much of the flux to the input, leaving a hollow in the center of the CPC.

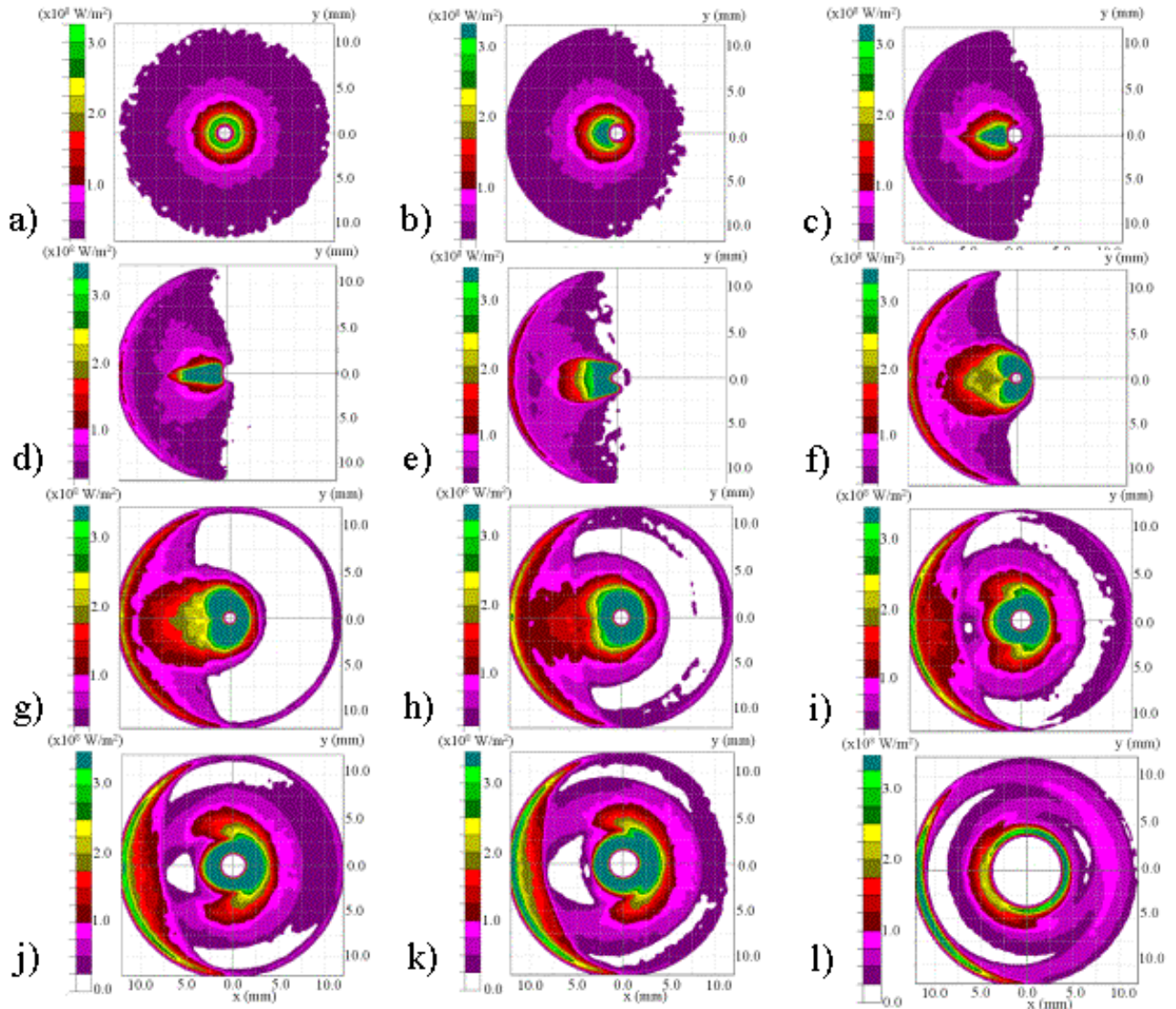


Figure 34. Maps of the projected flux density on the internal wall of the CPC for different values of incidence angle of the collimated beam: $\theta_{in} = 0.0^\circ$ (a); 1.0° (b); 2.0° (c); 3.0° (d); 4.0° (e); 5.0° (f); 6.0° (g); 7.0° (h); 8.0° (i); 9.0° (j); 10.0° (k); 20.0° (l). Wall reflectivity: $R_w = 0.9$

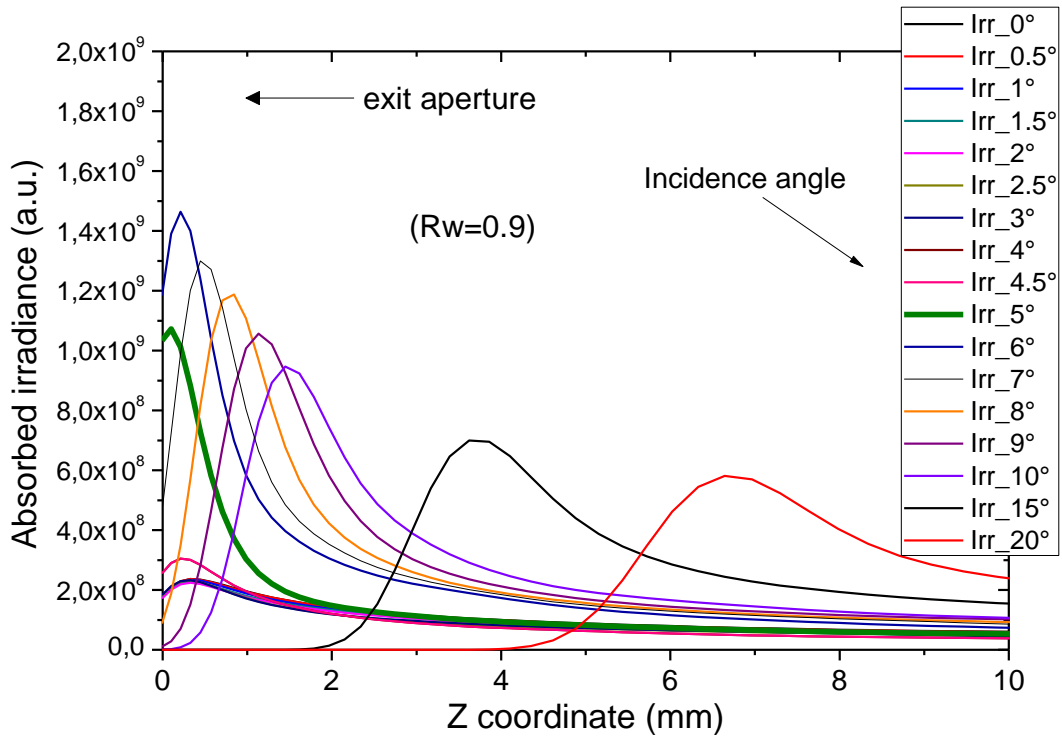


Figure 35. Distribution of the absorption irradiance along the optical axis, measured in a small portion (10 mm) of the CPC near the exit aperture ($z = 0$ mm). The absorption irradiance was obtained after rotational symmetrization of the maps of Fig. 34. Wall reflectivity: $R_w = 0.9$. The curve of $\theta_{in}=5^\circ$ (acceptance angle) is traced bold

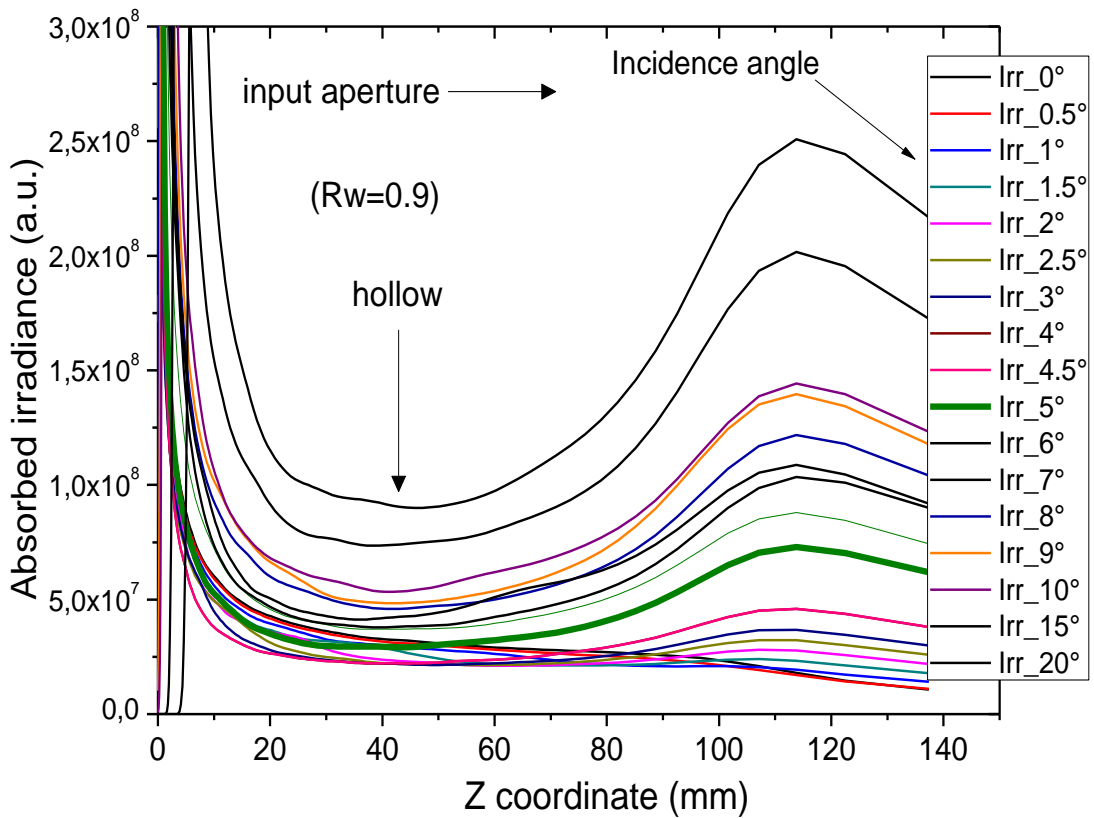


Figure 36. Distribution of the absorption irradiance along the optical axis, from $z = 0$ mm (the exit aperture) to $z = 150$ mm (the entrance aperture). The absorption irradiance was obtained after rotational symmetrization of the maps of Fig. 33. Wall reflectivity: $R_w = 0.9$. The curves of $\theta_{in}=5^\circ$ (acceptance angle) is in bold

6. Conclusions

In conclusion, we have presented in this work the results of optical simulations performed on a 3D-CPC nonimaging concentrator, irradiated in direct mode by a parallel beam, and imagined for photovoltaic applications. This simulation work is the first of a series discussing the practical application of the theoretical methods presented in the first part of this work[1]. Another series will regard the experimental application of those methods. The “direct” mode of irradiation is here distinguished by the “inverse” mode of irradiation which will be discussed in a forthcoming part of this work. After a brief discussion of the theory of the CPC, the 3D-CPC has been analyzed in extreme detail by using a ray-tracing program. We have explored its transmission properties, those of the most practical importance when the 3D-CPC is used in a PV solar system, in terms of transmission efficiency, spatial and angular distribution of the flux at the output. Generally of less importance is the study of its reflection and absorption properties. Nevertheless, we have dedicated a large part of this paper also to these aspects, applying the same methods used for the transmitted light, because it helps to understand the secret mechanism of light concentration in a CPC.

We summarize here the main results of the optical simulations.

i) We have presented the equation of the CPC profile expressed in cartesian coordinates, whereas generally it is expressed in polar coordinates.

ii) We have illustrated a general method for calculating the average number of reflections that the rays make within the CPC, which has been applied to the transmitted beam (2 reflections on average) and to the reflected beam (more than 5 reflections).

iii) We have investigated in detail the spatial distribution of output flux, identifying most of the peaks and their relative weight, as well as their origin from the input beam; the central intense peak is formed by a well defined annulus at input, whereas most of the output flux is concentrated on satellite peaks produced by rays close to the edge of input aperture.

iv) The study of angular divergence of the transmitted rays has proved useful to show that the rays on the solar cell diverge to a maximum of about 70°, which would make most of the commercial cells suitable to be applied directly on the CPC, but the flux density of the central peak is too high to be tolerated by a solar cell; the conclusion is that the CPC, like the one we have studied, is not suitable to be coupled directly to a solar cell. Remedies to this situation is the use of a secondary optical element, or the truncation and deformation of the CPC surface.

v) The study of the reflected and absorbed flux resulted useful from the educational point of view and for the development of new methods of optical investigation. Only a couple of issues, relative to the study of reflected rays, were not answered.

In conclusion, this in-depth study of the CPC concentrator,

we believe, will help to introduce into the routine work of the optical design new methods of simulation to be applied universally to the optical devices.

REFERENCES

- [1] A. Parretta, 2013, Optics of Solar Concentrators. Part 1: Theoretical Models of Light Collection, *Int. Journal of Optics and Applications*, Vol. 3, N. 4.
- [2] R. Winston, 1974, Principles of Solar Concentrators of a Novel Design, *Solar Energy* 16, 89-95.
- [3] W.T. Welford and R. Winston, 1978, *The Optics of Nonimaging Concentrators*, Light and Solar Energy, Academic Press.
- [4] W.T. Welford and R. Winston, 1989, *High Collection Nonimaging Optics*, San Diego, Academic Press.
- [5] A. Luque, 1989, *Solar Cells and Optics for Photovoltaic Concentration*, Adam Hilger, Bristol and Philadelphia.
- [6] R. Winston, J.C. Miñano, P. Ben fez, 2005, *Nonimaging Optics*, Elsevier Academic Press.
- [7] J. Chaves, 2008, *Introduction to Nonimaging Optics*, CRC Press.
- [8] J.J. O’Gallagher, 2008, *Nonimaging Optics in Solar Energy*, Morgan & Claypool Publishers, Lexington, KY.
- [9] A. Antonini, M.A. Butturi, P. Di Benedetto, D. Uderzo, P. Zurru, E. Milan, M. Stefancich, M. Armani, A. Parretta, N. Baggio, 2009, *Rondine® PV Concentrators: Field Results and Developments*, *Progress in Photovoltaics* 17, 451-459. ISSN: 1062-7995
- [10] A. Parretta, G. Martinelli, E. Bonfiglioli, D. Roncati, A. Antonini, M.A. Butturi, P. Di Benedetto, D. Uderzo, P. Zurru, E. Milan, *Indoor Optical Characterization of the Nonimaging “Rondine” PV Solar Concentrator*, in *Proceedings of the 24th EPSEC*, Hamburg, Germany, 21-25 September, 2009.
- [11] A. Parretta, G. Martinelli, A. Antonini, D. Vincenzi, *Direct and inverse methods of characterization of solar concentrators*, in *Proceedings of Optics for Solar Energy (SOLAR), Advancing the Science and Technology of Light*, The Westin La Paloma, Tucson, AZ, USA, June 7-10, 2010.
- [12] A. Parretta, A. Antonini, M.A. Butturi, P. Di Benedetto, D. Uderzo, P. Zurru, 2010, *Optical Methods for Indoor Characterization of Small-Size Solar Concentrators Prototypes*, *Advances in Science and Technology*, Trans Tech Publications, Switzerland, 74, 196-204.
- [13] A. Parretta, A. Antonini, M. Stefancich, V. Franceschini, G. Martinelli, M. Armani, 2007, *Characterization of CPC solar concentrators by a laser method*, in *Optical Modeling and Measurements for Solar Energy Systems*, ed. by Daryl R. Myers, *Proc. SPIE Vol. 6652*, pp. 665207 1-12.
- [14] A. Parretta, L. Zampierolo, D. Roncati, *Theoretical aspects of light collection in solar concentrators*, in *Proceedings of Optics for Solar Energy (SOLAR), Advancing the Science and Technology of Light*, The Westin La Paloma, Tucson, AZ, USA, June 7-10, 2010.

- [15] A. Parretta, P. Morvillo, C. Privato, G. Martinelli, R. Winston, Modelling of 3D-CPCs for concentrating photovoltaic systems, in Proceedings of PV in Europe, from PV Technology to Energy Solutions, Rome, Italy, 7-11 Oct. 2002 (WIP-Munich and ETA-Florence, 2002), pp.547-550.
- [16] A. Antonini, M. Stefancich, J.Coventry, A. Parretta, 2013, Modelling of compound parabolic concentrators for photovoltaic applications, Int. Journal of Optics and Applications, Vol. 3, N. 4.
- [17] <http://lambdares.com/>
- [18] D. Vincenzi, M. Stefancich, S. Baricordi, C. Malagù, M. Pasquini, F. Gualdi, G. Martinelli, A. Parretta, A. Antonini, Effects of irradiance distribution unevenness on the ohmic losses of point-focus and dense-array CPV systems, in Proceedings of the 24th EPSEC, Hamburg, Germany, 21-25 September 2009.
- [19] E.Franklin, J. Coventry, Effects of Highly Non-uniform Illumination Distribution on Electrical Performance of Solar Cells, ANZSES Solar Conference, 2002, Newcastle, Australia.
- [20] A. Antonini, M. Stefancich, D. Vincenzi, C. Malagà F. Bizzi, A. Ronzoni, G. Martinelli, 2003, Contact grid optimization methodology for front contact concentration solar cells, Solar Energy Materials and Solar Cells. 80, 155-166.
- [21] R. Leutz, A. Suzuki, A. Akisawa, T. Kashiwagi, Flux uniformity and spectral reproduction in solar concentrators using secondary optics, ISES Solar World Congress, Adelaide, 2001.
- [22] A. Parretta, G. Martinelli, M. Stefancich, D. Vincenzi and R. Winston, Modelling of CPC-based photovoltaic concentrator, in: Proc. of SPIE, Vol. 4829, 2003, pp. 1045-1047.
- [23] R. Leutz, A. Suzuki, A. Akisawa, T. Kashiwagi, Flux uniformity and spectral reproduction in solar concentrators using secondary optics, ISES Solar World Congress, Adelaide, 2001.
- [24] H. Ries, J.M. Gordon, M. Lasken, 1997, High-flux photovoltaic solar concentrators with kaleidoscope-based optical designs, Solar Energy 60, 11-16.
- [25] M.M. Chen, J.B. Berkowitz-Mattuck, P.E. Glaser, 1963, The Use of a Kaleidoscope to Obtain Uniform Flux Over a Large Area in a Solar or Arc Imaging Furnace, Applied Optics 2, 265-272.
- [26] K. Kreske, 2002, Optical design of a solar flux homogenizer for concentrator photovoltaics, Applied Optics 41, 2053-2058.
- [27] R. Winston, R. C. Gee, Nonimaging light concentrator with uniform irradiance, US Patent 6,541,694 B2, April 1, 2003.
- [28] A. Parretta, A. Sarno, P. Tortora, H. Yakubu, P. Maddalena, J. Zhao, A. Wang, 1999, Angle-dependent reflectance measurements on photovoltaic materials and solar cells, Optics Communications 172, 139-151..